Received: 10 April 2020 | Revised: 4 November 2020 | Accepted: 18 November 2020 | Published on: 19 January 2021

DOI: 10.1002/qj.3955

Quarterly Journal of the Royal Meteorological Society RMetS

RESEARCH ARTICLE

Understanding mechanisms for trends in Sahelian squall lines: Roles of thermodynamics and shear

Megan E. Bickle[1] | **John H. Marsham**[2,3] | **Andrew N. Ross**[2] | **David P. Rowell**[4] | **Douglas J. Parker**[2] | **Christopher M. Taylor**[5,6]

[1]Fluid Dynamics CDT, University of Leeds, Leeds, UK

[2]School of Earth and Environment, University of Leeds, Leeds, UK

[3]National Centre for Atmospheric Science (NCAS), Leeds, UK

[4]Met Office, Exeter, UK

[5]UK Centre for Ecology and Hydrology, Wallingford, UK

[6]National Centre for Earth Observation, Wallingford, UK

Correspondence

M. Bickle, EPSRC Centre for Doctoral Training in Fluid Dynamics, University of Leeds, Leeds, UK

Email: scmeb@leeds.ac.uk

Funding information

EPSRC, University of Leeds CDT in Fluid Dynamics, Grant/Award Number: EP/L01615X/1; Future Climate for Africa AMMA2050 and IMPALA projects, Grant/Award Numbers: NE/M020126/1, NE/M017214/1, NE/M020428/1; GCRF African SWIFT, Grant/Award Number: NE/P021077/1; National Centre for Atmospheric Science via the NERC/GCRF program, Atmospheric hazards in developing countries: risk assessment and early warning; UK NERC/Department for International Development FCFA programme, under the AMMA-2050 project, Grant/Award Number: NE/M019977/1; NERC GENESIS and ParaCon programme, Grant/Award Number: NE/N013840/1

Abstract

Squall lines dominate rainfall in the West African Sahel, and evidence suggests they have increased in intensity over recent decades. Stronger wind shear may be a key driver of this trend and could continue to strengthen with climate change. However, global numerical models struggle to capture the role of shear for organised convection, making predictions of changing rainfall intensities in the Sahel uncertain. To investigate the impact of recent and possible future environmental changes, and to isolate thermodynamic effects from shear effects, idealised squall line simulations were initialised with a profile representative of the present day: this profile was then modified using trends from reanalyses and climate projections. Increased shear led to increased storm intensity and rainfall, but the effects of the thermodynamic changes dominated the effects from shear. Simulations initiated with future profiles produced shorter-lived storms, likely due to increased convective inhibition and the absence of large-scale convergence or synoptic variability in the idealised model. A theoretical model based on the relative inflow of convectively unstable air and moisture was found to predict bulk characteristics of the storms accurately, including mean rain rates and area-averaged maximum vertical velocities, explaining the role of shear. However, the model is not a prognostic tool as rainfall is dependent on the storm speed, which remains a free parameter. The study shows the importance of shear to long-term rainfall trends and highlights the need for climate models to include effects of shear to capture changes in extreme rainfall.

KEYWORDS

climate change, mesoscale convective systems, West African Monsoon

1 | INTRODUCTION

The Sahel has one of the largest and fastest-growing populations in Africa, large portions of whom are dependent on subsistence farming and consequently the seasonal rains. The West African Monsoon (WAM) dominates the climate of this region, with most of the rainfall delivered by mesoscale convective systems (MCSs; Lebel *et al.*, 2003). The MCSs are often in the form of squall lines, and the Sahel experiences some of the most regular and severe squall lines on Earth. When these convective events are at their most extreme, the resulting flooding can be destructive for both agricultural land and urban areas. Once deep moist convection has formed in the WAM, it can, to a large extent, self-organise. On such occasions, long-lasting deep convective motions can be sustained in the absence of mesoscale forcing (Fink and Reiner, 2003).

The WAM is a response to the Saharan heat low which forms during the summer as the Sahara is heated intensely (Lavaysse *et al.*, 2009). The south-westerly monsoon winds, which bring moisture from the Gulf of Guinea, are strongest at night; the cooling surface reduces dry convection, and the wind strengthens as turbulence lessens and the boundary layer shrinks (Parker *et al.*, 2005a). Above the monsoon boundary layer, the African Easterly Jet (AEJ) reaches its maximum at 600–700 hPa (Burpee, 1972). Moist convection is predominant equatorward of the jet, whereas dry convection, and the markedly warmer and drier Saharan air layer (SAL), define the region northward (Parker *et al.*, 2005b; Stein *et al.*, 2011). There is an important transition zone where the shallow monsoon layer undercuts the SAL, creating a situation of high convective inhibition (CIN) and a build-up of convectively available potential energy (CAPE). The SAL creates dry mid-levels which are thought to enhance downdraughts and so produce stronger cold pools (Parker *et al.*, 2005b; Takemi, 2006). The transition from the south-westerly monsoon winds nearer the surface to the AEJ produces wind shear, which is strongest at night, and which supports squall-line MCSs, which tend to initiate in the afternoon or evening and then persist overnight (Browning and Ludlam, 1962; Ludlam, 1963; Roca *et al.*, 2005; Lebel *et al.*, 2010). The speed of MCS cloud lines can vary greatly, and they are categorised as fast-moving and thus squall lines if they travel at over 7 $\mathrm{m \cdot s^{-1}}$. Observations have suggested that the faster-moving squall lines develop in environments which have drier mid-levels and where the vertical shear of the horizontal wind is normal to the leading edge of the squall line (Barnes and Sieckman, 1984). Taylor *et al.* (2017) found a correlation between storm intensity and propagation speed (PS), with MCSs categorised as the most extreme travelling at mean speeds of 18.3 $\mathrm{m \cdot s^{-1}}$.

The convection parametrisations used in global models struggle to capture deep moist convection, leading to systematic errors in both global numerical weather prediction and climate models (Peters *et al.*, 2019; Kniffka *et al.*, 2020). For the Sahel, this is due to the convection parametrisation schemes that represent deep moist convection triggering too easily and typically lacking any representation of organisation. This results in the numerical models predicting the rainfall peak too early in the day and the rain too widespread, not producing storms which sustain past sunset and failing to capture the most intense rainfall (Stephens *et al.*, 2010). The repercussions of an incorrect representation of the diurnal cycle impact the entire monsoon system, including pressure gradients, winds and the water budget (Marsham *et al.*, 2013; Birch *et al.*, 2014). Other aspects of convection which are not realistically modelled include organisation, cold pool initiation, land surface impact (Garcia-Carreras *et al.*, 2013; Taylor *et al.*, 2013; Trzeciak *et al.*, 2017) and, key to the efforts in this work, the effects of wind shear.

Panthou *et al.* (2014) studied climatic trends for the Sahel by considering data from over 700 weather stations and validating against 43 that were continuously operated from 1950 to 2010. They concluded that, over the period of 2001 to 2010, the Sahelian region was characterized by a more extreme climate, with a proportion of annual rainfall associated with extreme rainfall of 21%, compared with 17% in the 1970–1990 period. The climate was drier in the sense of a persisting deficit in rainfall occurrence compared with 1950–1969, while at the same time there was an increased possibility of extreme daily rainfall. This was corroborated by Taylor *et al.* (2017), who used 35 years of satellite observations and rain gauge readings from the West African Sahel to reveal a persistent increase in the frequency of the most intense MCSs over this period: this was inferred from a trend of −0.78 °C/decade in cloud top temperatures. Intensification of MCSs was restricted to a narrow Sahelian belt in the months of June to September but extends to the Guinea coast in the spring (Klein *et al.*, 2021). This increase in the frequency of MCSs is only weakly related to the multi-decadal recovery of the Sahel annual rainfall but exhibits a similar trend to global land temperatures.

Taylor *et al.* (2017) calculated zonal means across 15 °E– –15 °W of atmospheric variables from European Centre for Medium-Range Weather Forecasts (ECMWF) ERA-Interim Reanalysis data (ERA-I). On considering the latitudes 5–25 °N within the longitudes stated, they found correlations at both event and inter-annual time scales between storm intensity and increased Sahelian temperatures, drying at mid-levels and stronger wind shear. The correlating rising temperatures were within the Saharan planetary boundary layer (PBL) as well as the SAL which overlies the Sahelian PBL. This increase in temperatures results in a corresponding thermal wind which strengthens the AEJ, while the warmer (and deeper) Saharan heat low strengthens monsoon flow. Taylor *et al.* (2017) found no observable accompanying trend of increased precipitable water or specific humidity and concluded that the increase in wind shear has contributed to the observed rise in MCS intensity. Recent work exploring climate change projections over Africa using convection permitting, finer resolution (4.5 km) models (CP4A) has suggested that dry and wet extremes over West Africa are expected to intensify in the future (Kendon *et al.*, 2019). Through analysing CP4A data, Fitzpatrick *et al.* (2020) found that rain rates scaled with the product of time-of-storm total column water and in-storm vertical velocity. However, despite pre-storm wind shear modulating in-storm vertical velocity and the resulting cloud-top temperatures, they found no direct correlation between wind shear and precipitation rates in CP4A, in contrast to observations for the Gulf of Guinea (Klein *et al.*, 2021).

Strong shear at low levels, perpendicular to the convective line, can encourage squall line intensity and longevity (Browning and Ludlam, 1962; Ludlam, 1963). Rotunno *et al.* (1988) discuss the dynamic role that environmental wind shear plays in controlling the resulting cold pool of a thunderstorm and its interaction with the environment. This interaction produces more vertical lifting and therefore deeper convection than would be possible without the low-level shear, such that new cells form and grow more easily as old cells decay. According to this model, optimal lifting of near-surface parcels requires a balance between the intensity of the cold pool and environmental shear. However, although optimal, these conditions are not necessary for convective systems to be intense or long lived (Bryan *et al.*, 2006). Additional considerations which impact the cold pool/wind shear interaction include: gust front-relative surface (elevated) rear-inflow jets, which can contribute to (counteract) the cold pool circulation (Weisman, 1992), the impact of the cold pool inducing accelerations beyond its confines (Weisman and Rotunno, 2004) and the interaction of mid- and upper-level shear with convective updraughts (Fovell and Tan, 1998; Parker and Johnson, 2004). Alfaro and Khairoutdinov (2015) suggest that variations in the intensity of squall lines have been wrongly attributed to vorticity balance, particularly as latent heating often depends on shear strength. Alfaro (2017) developed the Layer Lifting Model of Convection (LLMC), a theoretical model based on the premise that low-level shear modulates the system-relative inflow of both convectively unstable air and water vapour. This theory places importance on the thermodynamic role that wind shear can play in deep moist convection but so far has only been tested for mid-latitude conditions and for cases of idealised shallow shear.

Dry air aloft can have a key role in convection, in particular the influence of mid-level dry air on the production of cold pools and the overall strength of squall lines. Even in environments with identical CAPE and vertical wind shear, varied mid-tropospheric dryness can cause significant differences in the morphology and evolution of convective storms. For supercell storms, low relative humidity above the cloud base aids the formation of strong downdraughts through evaporation (Gilmore and Wicker, 1998). However, in the tropics, dry air aloft has been found to suppress convection due to the detrimental effects of dry air on entrainment (Brown and Zhang, 1997). Through idealised large-eddy simulation (LES) experiments, James and Markowski (2010) found that dry air aloft reduced the intensity of convection measured by upward mass flux and total condensation, although this was inconsequential for high-CAPE (in excess of $4,000\,\mathrm{J{\cdot}kg^{-1}}$) line-type scenarios where downdraught mass flux and cold pool strength were enhanced but only in the trailing stratiform region. In the Sahel, cold pools are stronger pre-monsoon than in the monsoon season, and evidence suggests that drier mid-levels play an important role (Provod *et al.*, 2016).

Several previous studies have tested the validity of different spatial resolutions for simulating convection (Bryan *et al.*, 2003; Bryan and Morrison, 2012) with a general consensus that, below a horizontal resolution of $\mathcal{O}(500\,\mathrm{m})$, the peak in the vertical velocity energy spectrum is resolved (Lebo and Morrison, 2015). Simulations with horizontal grid spacing of $\mathcal{O}(1\,\mathrm{km})$ produce systems with larger convective cells that do not entrain mid-level air and so produce more precipitation and have higher cloud tops (Bryan and Morrison, 2012). Bryan *et al.* (2003) also list precipitation distribution and amount as well as convective cell structure, system phase speed and the organisational mode of convective overturning as inconsistencies between simulations with horizontal grid spacing $\mathcal{O}(1\,\mathrm{km})$ versus $\mathcal{O}(100\,\mathrm{m})$. The coarser grid of 1 km is robust for processes such as gravity currents and net momentum and heat transports (Weisman *et al.*, 1997).

In summary, past observational studies implicate decadal trends in Sahelian temperature and its impact on vertical wind shear in the recent intensification of MCSs in the Sahel, but previous modelling has not captured this (Fitzpatrick *et al.*, 2020) and several theories exist for the role that shear plays in deep moist convection. In particular different theoretical models disagree over whether shear plays a dynamical role through balancing the cold pool or a thermodynamic one through modulating the system-relative inflow of convective instability and moisture. In this study, we use idealised simulations of squall lines to bridge the gap between observations and theory and to shed some light on the fundamental processes. Through initiating simulations with representative profiles from observations, modified by changes derived from long-term trends in reanalyses or future climate projections, we isolate and examine how changes to the environmental wind or thermodynamic profile can affect the intensity of convection. The study has four main hypotheses that we test: (a) recent increases in shear from both strengthened monsoon south-westerlies and the AEJ, caused by Saharan warming, have increased the intensity of squall lines (Taylor *et al.*, 2017), (b) recent changes to the environmental thermodynamic profile may have influenced squall line intensity and could be comparable to the effects of shear, (c) the system-relative inflow of CAPE and water vapour is key to determining squall line updraught speeds and rainfall so that the LLMC can explain the modelled impacts of changing profiles and (d) predicted future increases in shear, temperature and humidity will cause an increase in storm intensity.

Our study uses idealised LES experiments to investigate the impact of changing environmental thermodynamic and wind profiles on squall lines representative of those seen in the West African Monsoon. Section 2 outlines the control profile that is used and the sensitivity simulations based on historical and future climate changes. The changes considered are those from reanalysis from the period of 1982 to 2017 to allow comparison with the results of Taylor *et al.* (2017). We test whether our idealised simulations produce changes in storm intensity that are consistent with those discussed in Taylor *et al.* (2017) from a small environmental change taken from trends in reanalyses. Further experiments consider possible future changes to squall line intensity by adding, to our control profile, environmental changes predicted by the Coupled Model Intercomparison Project 5 (CMIP5) for the end of this century under a high-emissions scenario to explore possible future impacts on this vulnerable region. The LLMC is discussed in Section 2.5 and is applied to our LES results to investigate whether it successfully captures variations in modelled squall line intensities. This is a recent theory, and in this paper, we perform a unique test of this model in tropical conditions. Section 3 discusses the relative roles of wind shear and thermodynamic environments on squall lines and whether the LLMC is consistent with the changes in squall line characteristics seen in the results from the idealised simulations. Finally, Section 4 presents some conclusions.

2 | METHODS

2.1 | Experimental setup

2.1.1 | Numerical model: “Cloud Model 1”

Numerical three-dimensional simulations of idealised squall lines were performed using Cloud Model version 18 (Bryan and Fritsch, 2002). The advection of velocities and scalars is integrated with fifth-order horizontal and vertical advection schemes with implicit diffusion, with a Klemp–Wilhelmson time-splitting, vertically implicit, horizontally explicit pressure solver. The domain extends 1,600 × 60 km in the horizontal (across squall line, x, and along squall line, y, directions) with 1 km grid spacing. Horizontal boundaries are open in the across-line (west to east) direction and periodic in the along-line direction. The Durran–Klemp formulation (Durran and Klemp, 1983) is employed for the open-flow boundaries and allows gravity waves to exit the computational domain with minimal reflection. The periodic boundary conditions in the along-line direction allow the squall line to extend across the entire domain in this direction. In the vertical, the domain is 23.4 km deep. The vertical grid stretches from 25 m spacing at the surface to 500 m at 8.4 km and above, resulting in 62 vertical levels. The lower boundary condition is set to a flat, rigid surface, while a free-slip boundary condition is applied to the top of the domain, with a Rayleigh damping sponge layer above 20 km. Micro-physics processes are parametrised with a version of the Morrison double-moment scheme (Morrison *et al.*, 2005) which predicts number concentrations and mixing ratios of cloud droplets, cloud ice, rain, snow and hail. No radiation and surface heat and moisture fluxes are included in simulations shown here, both to aid the isolation of the role of shear and since the simulations were intended to represent nocturnal squall lines. The simulations were initialised with a horizontally homogeneous profile (Section 2.2), with storms triggered by a cold line thermal (Section 2.2.1).

2.2 | Control profile

The available historical reanalyses and predictions from models contain systematic biases. To minimise inaccuracies, observational data are used as the basis of the control profile for the model and only changes over time are derived from reanalyses and climate projections.

The initial conditions used as a control, see Figure 1, were taken from radiosonde measurements made during

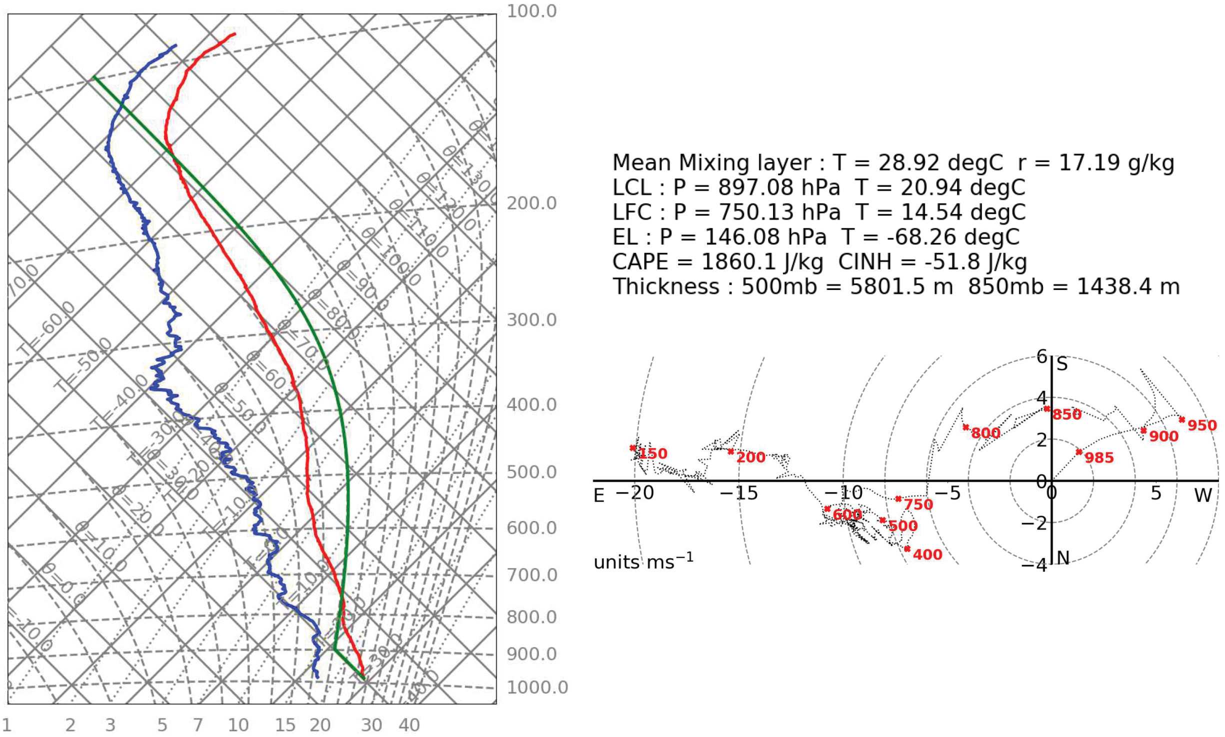

FIGURE 1 Tephigram and hodograph of the control profile created from selecting the top 25% of profiles with the highest CAPE and lowest CIN and finding the average. The selections were made from evening, night and early morning (1800, 0000 and 0600 UTC) radiosonde profiles from 12 hrs before cold pools were recorded at Niamey in July and August 2006. On the tephigram, the units are hPa for the *y*-axis, g·kg^{-1} for the *x*-axis and ° for all temperatures shown. Wind direction on the hodograph represents winds from that direction

the AMMA 2006 field campaign (Parker *et al.*, 2008). The data used in this project are from Niamey in Niger, latitude 13° 29′N and longitude 02 °10′E. Niamey lies in a flat region west of mountains and so is fairly, but not completely, representative of the wider Sahel. However, these are by far the most comprehensive observations of the atmospheric profile over West Africa, a region where analyses exhibit major biases (Roberts *et al.*, 2015).

As the simulations are idealised and it is the variations from the control run that are of real interest, we deemed that a realistic profile based on observations that are representative of the wider Sahel was the best approach for the control run. Furthermore, as sustained MCSs are mainly initiated in the evening and continue overnight, only nocturnal and early morning profiles (1800, 0000 and 0600 UTC) from July and August were considered. As simulations are only run for 8 hrs these profiles are representative of this period. To produce an atmospheric profile representative of those in which squall lines were observed to occur, only soundings from the 12 hrs immediately before cold pools passed over Niamey, as identified by Provod *et al.* (2016), were considered. Finally, the control profile was created from selecting the top 25% of pre-storm nocturnal profiles with the highest CAPE and lowest CIN and finding the average. This mean profile, Figure 1, has a CAPE of 1,860 J·kg^{-1} and CIN of 52 J·kg^{-1}. There is a decrease in humidity from 750 to 600 hPa which is indicative of the SAL. The hodograph shows south-westerly winds above the surface with the nocturnal low-level jet spanning from 960 to 900 hPa with a peak in westerlies at 950 hPa. Above 900 hPa there is a continuous decrease in westerly winds while southerly winds sustain around 3.8 m·s^{-1} until 800 hPa, when they start to weaken. The AEJ spans from 725 hPa to a maximum at 600 hPa, which can more easily be seen in Figure 2. It is also worth noting the easterly winds above 250 hPa as these control the spread of the cloud anvil.

The CAPE and CIN (calculated for parcels of air at different height levels of the profile) and water vapour mixing ratio (WVMR) are shown in Figure 2. There is moist air with CAPE from the surface to above the surface air's Lifting Condensation Level (LCL) at 900 hPa and just below the surface air's Level of Free Convection (LFC). The system-relative wind speed is also plotted and shows that the majority of the inflowing air comes from below 750 hPa and particularly at the height of the low-level jet. Although the CAPE of the air above 800 hPa is zero, there is still moisture flowing into the storm at this level.

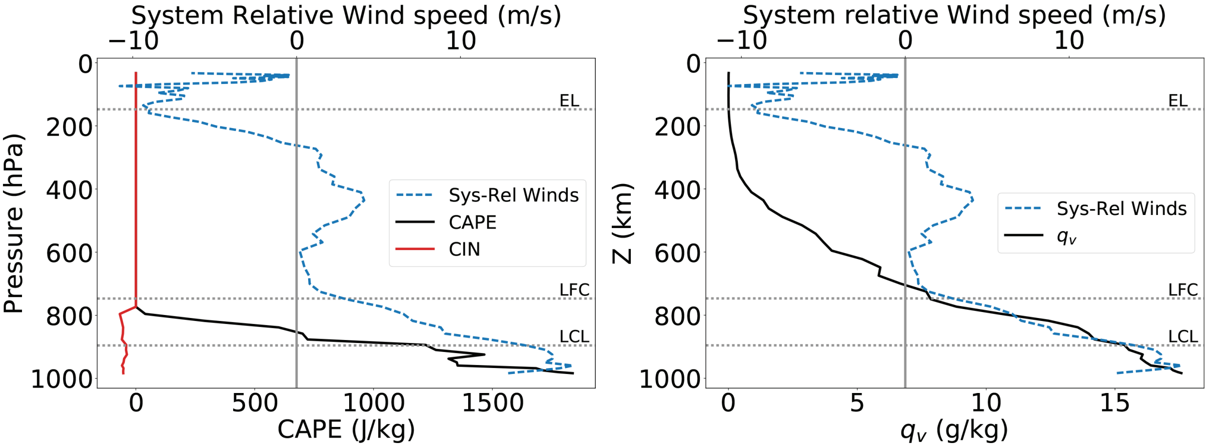

FIGURE 2 The CIN, CAPE and WVMR at different heights for the control profile. The LCL, LFC and equilibrium level (EL) for a parcel at the surface are marked. The system-relative wind speed at each level is relative to a system speed of $-10.7\,\mathrm{m{\cdot}s^{-1}}$

2.2.1 | Initiation

The squall line is initiated with an elevated north–south line thermal, to produce a line of convection. The perturbation has a maximum amplitude of -2 K located at 3 km above ground and at 910 km on the x-axis. The perturbation has a horizontal half-width, x_r, in the x-direction of 40 km and a vertical half-width of $z_\mathrm{r} = 3$ km. The temperature perturbation of the line thermal is at a maximum at the centre, (x_0, z_0), and decreases to zero at the edges with a sinusoidal shape determined by $\cos^2(\frac{\pi}{2}\beta)$ where $\beta = \sqrt{(\frac{x-x_0}{x_\mathrm{r}})^2 + (\frac{z-z_0}{z_\mathrm{r}})^2}$. A random seed number generator is used to add random noise of maximum amplitude 0.2 K to the line thermal perturbation at every point to allow three-dimensional flows to develop. Simulations were repeated five times with different random seeds so that each experiment had unique small-scale random noise within the same overall line thermal temperature perturbation. This allowed separation of effects of random variations from those resulting from changes to the environmental profile. Over the remainder of the domain, the initial conditions are horizontally homogeneous.

There was some difficulty in producing squall lines that reached a steady state for the thermodynamic profile measured during the AMMA campaign with average CMIP5 changes added on. Warm and cold line thermals of varying temperatures were tested to explore whether the unexpectedly quick demise of the storms was a consequence of the initiation or could be considered a characteristic of the environmental changes predicted across the CMIP5 models. We conclude that the thermodynamic profile with the predicted CMIP5 changes applied is not conducive to producing long-lasting storms in this simple experiment, which could be due to a lack of large-scale flows to sustain convergence and triggering, although lack of representation of radiation or synoptic variability may also be important. The triggering that was eventually chosen for all the results discussed in this paper is the single cold line thermal of 2 K perturbation described in the previous paragraph, which produced the longest-lasting storms.

As there were concerns over the validity of using a horizontal grid spacing of 1 km, the control and the ERA-Interim cases were run on a finer grid where the horizontal spacing was 200 m with a vertical resolution of 15 m at the surface that stretched to a constant spacing of 250 m from 8.5 km. Due to computational constraints, only one of the random seeds was tested. The statistics from these experiments were then compared with experiments using the standard grid and a coarser version still: 2 km in the horizontal. The limited effects of the varied grid spacings, which are discussed further in Section 3.3, gave reassurance that our conclusions are not affected by such variations in grid spacing.

2.3 | Past decadal trends in thermodynamics and shear from ERA-Interim analyses

Having obtained a realistic and representative profile of the Sahel region from radiosondes taken at Niamey, we now consider how that profile may have changed over recent decades. To allow comparison with Taylor *et al.* (2017) and test hypothesis 1, changes in the mean profiles of WVMR, potential temperature and horizontal winds over the period 1982–2017 were calculated using the months of June to September at 1200 UTC across 15 °E–15 °W and 16–17 °N from ERA-I reanalysis data. Higher latitudes than that of Niamey were used for the

TABLE 1 The number of repeated experiments run for each wind and thermodynamic profile combination

		Thermodynamics		
		Control (2000s)	**ERA-I (1980s)**	**CMIP5 (2100s)**
Winds	Control (2000s)	5	5	5
	ERA-I (1980s)	5	5	—
	CMIP5 (2100s)	5	—	5

Note: Each profile combination was run five times with a different random seed generator to produce unique random noise at every point in the line thermal perturbation.

reanalysis data as the strongest trends in variables and strongest correlations with MCS intensity exist between 15 and 20 °N. Applying these changes to our control allows direct comparison with the changes considered by Taylor *et al.* (2017) and a means of testing their suggestion that increases in westerly wind speeds of 0.4 $\mathrm{m{\cdot}s^{-1}}$ $\mathrm{decade^{-1}}$ in the lower troposphere from 15 to 22 °N caused higher wind shear and correlated most significantly with MCS intensity across the region. Additionally, the highest correlation between increases in mid-level temperatures and MCS intensity were found at similar latitudes. Once the linear ERA-Interim changes were calculated for each of the variables, the profiles were interpolated onto the finer grid of the AMMA control profile using cubic interpolation. A profile representing the 1980s conditions was then obtained by deducting the change from the control profile. The experiments run are listed in Table 1.

Figure 3 shows changes in winds and humidity in ERA-Interim from 1982 to 2017 at selected pressure levels across the wider region. Low-level moisture has increased north of Niamey while decreasing around Niamey (Figure 3a), consistent with an increase in the low-level south-westerly monsoon winds north of Niamey (Figure 3d). Changes in the AEJ west of 10 °E are small, with a weak, 1.4 $\mathrm{m{\cdot}s^{-1}}$ increase in the AEJ north of Niamey (Figure 3b). There is an increase in the magnitude of the shear vector (Figure 3c) of 0.9×10^{-3} $\mathrm{s^{-1}}$ north of Niamey (16 to 18 °N) and a smaller change of 0.2×10^{-3} $\mathrm{s^{-1}}$ around Niamey (10 to 14 °N). Within the marked white box, (15 °E–15 °W and 16–17 °N), there is an increase in low-level WVMR and shear (Figures 4a and 5).

Baroclinicity and day-to-day variability are characteristic of the Sahel region. Both factors matter and can cause changes in the environmental profile in the same zone on the same day. Given the innate uncertainty across the region, the changes calculated from the ERA-Interim data for 16–17 °N can be interpreted as plausible ranges for each parameter over this period. Additionally, they are some of the more extreme variations within the ERA-Interim data for the Sahel area and thus provide a higher signal-to-noise ratio in our idealised simulations. The validity of the ERA-Interim data will be considered in Section 3.4 when compared with alternative reanalyses for the same region.

The AMMA control profile is compared against the same with the ERA-Interim changes subtracted in Figure 4a. The buoyancy profile change is negative throughout, such that the 2006 profile has both higher CIN and lower CAPE compared with the 1980s. This suggests that storms are more likely in the 1980s profile and could also be more intense. Figure 5 shows that, from the 1980s to the 2006 control profile, there is an increase in the westerly component of the low-level monsoon winds of 1.8 $\mathrm{m{\cdot}s^{-1}}$ as well as a slight increase of 0.4 $\mathrm{m{\cdot}s^{-1}}$ in the AEJ at 600 hPa. Also evident is an increase in shear since the 1980s. The changes to the southerly component of the winds are less marked with only an increase of 0.18 $\mathrm{m{\cdot}s^{-1}}$ in the monsoon winds and a decrease of 0.57 $\mathrm{m{\cdot}s^{-1}}$ in the northerly component of the AEJ. To conclude, the 2006 profile has higher CIN, lower CAPE and increased shear compared with the profile representative of the 1980s.

2.4 | CMIP5 predicted change

Monthly profiles were obtained from 34 CMIP5 models (Taylor *et al.*, 2012) representing both the historical (1950–1999 average) case and a predicted future (2070–2099 average) case from Representation Concentration Pathways scenario 8.5 (RCP8.5). The RCP8.5 scenario was chosen as it represents high future emissions and large global temperature change and thus provides a good signal-to-noise ratio.

The CMIP5 models provide our best current estimate of possible changes for this emissions scenario and our best method of testing hypothesis 4. The changes from CMIP5 were applied to the control profile; this is preferred to studying the actual profiles as the CMIP5 models have significant biases. Thermodynamic and wind changes were applied individually and together to study the effect each has independently and when combined.

The CMIP5 profiles studied are averages for the months of July and August for a 3×3 grid box around Niamey for the two time periods, using the temperature, specific humidity and horizontal winds at 11 pressure levels and the temperature and specific humidity at the surface. The average across models for each time period was calculated, and the mean change predicted found

(a) Mixing Ratio at 850hPa

(b) Horizontal winds at 600hPa

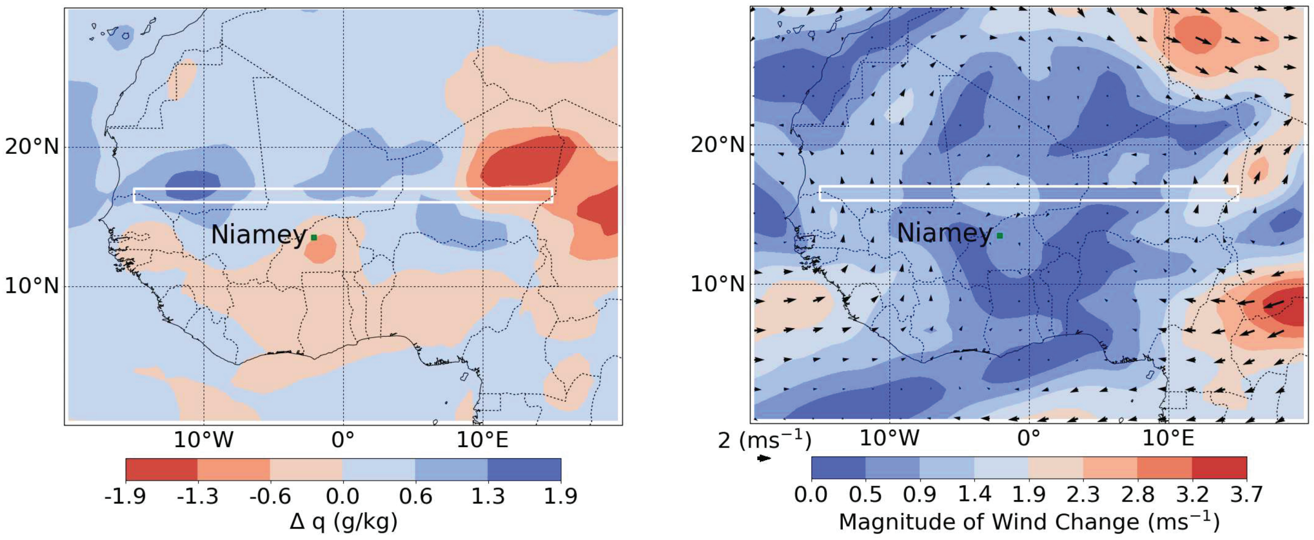

(c) Wind Shear (600-925)hPa

(d) Horizontal Winds at 925hPa

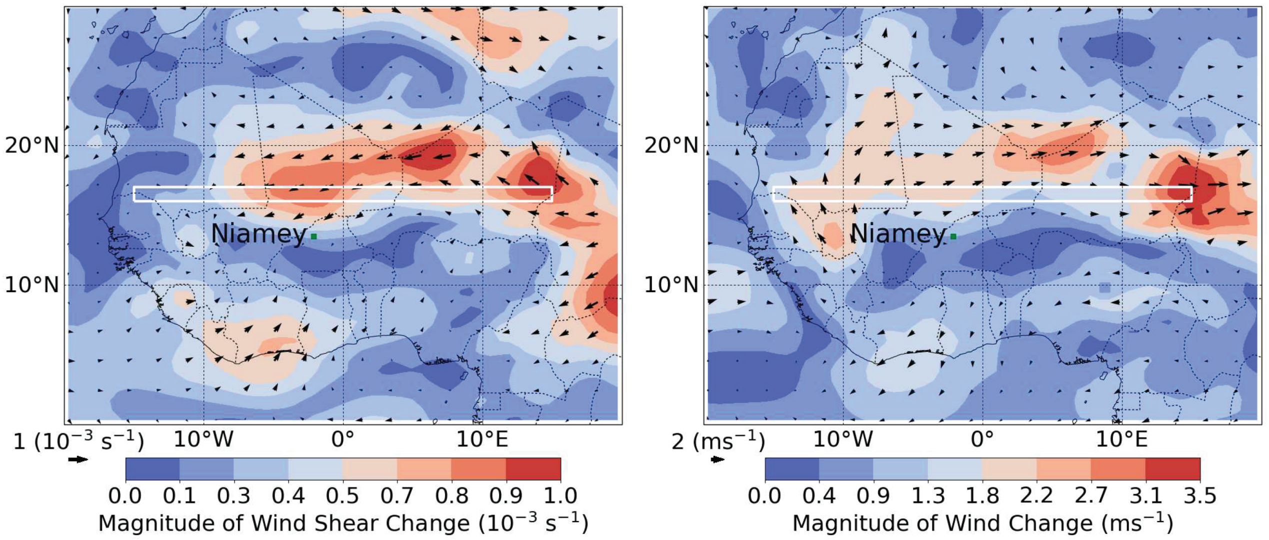

FIGURE 3 Linear trend calculated from an annual mean from 1982 to 2017 of ECMWF ERA-Interim reanalysis data at 1200 UTC over the months of June to September. The white box, 15 °W–15 °E and 16 °–17 °N, defines the region used to determine the final change applied to the control profile

from these averages. The average changes for potential temperature, humidity and wind were interpolated onto the higher-resolution grid of the AMMA control profile using cubic interpolation. The different variations of the control profile with the CMIP5 environmental changes applied were simulated and repeated with five different random seeds (Table 1).

The AMMA control profile is plotted against the control with the CMIP5 changes applied in Figure 4b. The buoyancy profile change is negative near the surface but positive above the level of free convection, showing increased CAPE and increased CIN in our future profile. From this, it can be anticipated that convection is less likely to occur in the future, but when it does it will be more extreme. At the same time, Figure 6 shows an increase in the low-level monsoon winds of 1.8 m·s^{-1} in the westerlies of the future profile as well as an increase of 1 m·s^{-1} in the AEJ at 500 hPa. There is an increase in both wind magnitudes, in opposite directions, at the altitudes mentioned, and thus shear increases compared with the current profile. There is also some indication that the maximum of the AEJ may extend higher in the

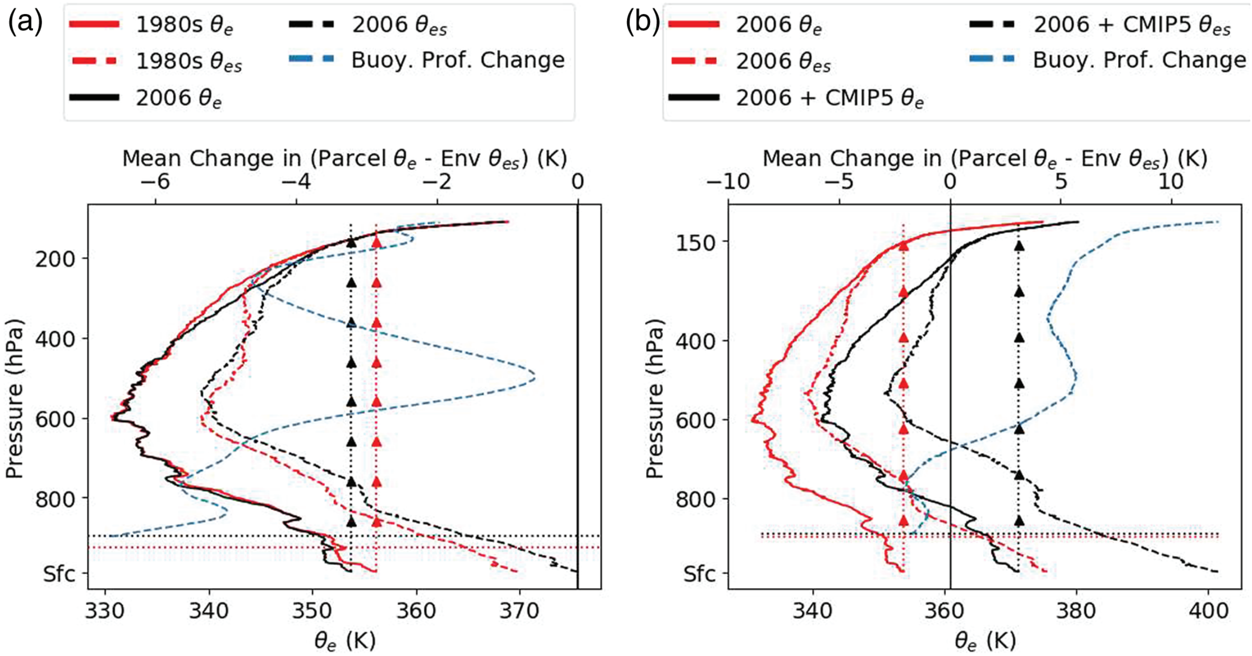

FIGURE 4 Average equivalent potential temperatures across past (red) and future (black) for the Niamey region. The comparisons include the 2006 control profile obtained from the AMMA campaign and (a) the linear trend of ECMWF from 1982 to 2017 deducted from it and (b) the average calculated change across CMIP5 models applied. The saturated equivalent potential temperature is plotted dashed, while the vertical lines indicate the equivalent potential temperature of a surface parcel. The horizontal dotted lines mark the lifting condensation level. The blue dashed line represents the change in buoyancy profile (buoyancy calculated as the difference between a surface parcel's θ_e and the environment θ_{es} at levels above the LCL)

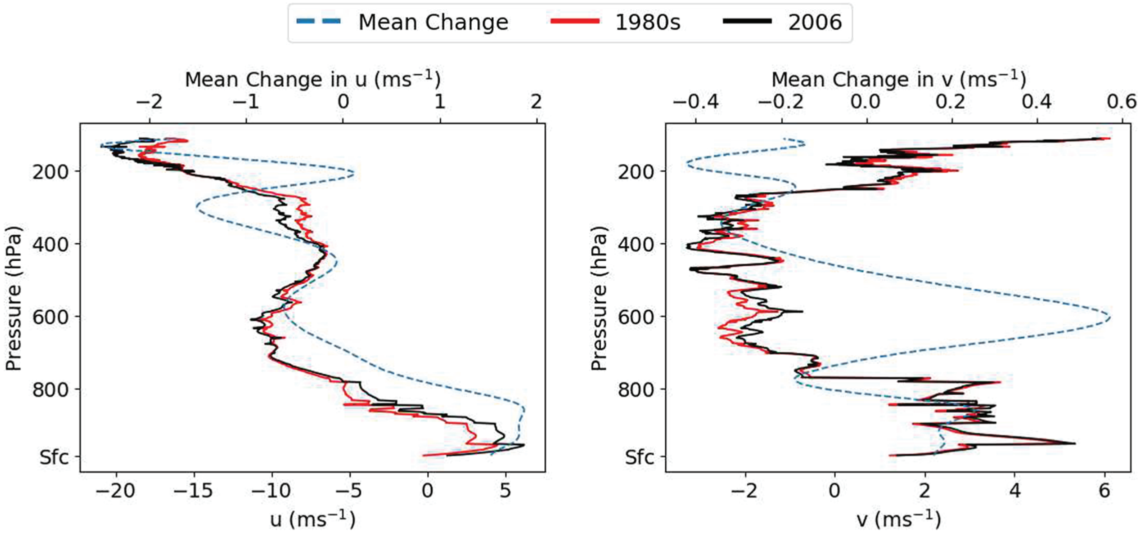

FIGURE 5 Control profile (black) for u and v with the ERA-Interim reanalysis trend from 1982–2017 deducted (red). The change between profiles is shown in blue (dashed)

future or that the maximum is predicted at varied altitudes between CMIP5 models. However, as can be seen from the standard error of the average across the different models, there is uncertainty in these predictions. In some cases, this includes disagreement between models over whether the change in a variable will be of positive or negative sign.

2.5 | Layer lifting model of convection

In this section, we describe the LLMC developed in Alfaro (2017), which is tested, with hypothesis 3, in Section 3.2. The model provides an indication of the intensity of deep convection given initial thermodynamic and dynamic conditions.

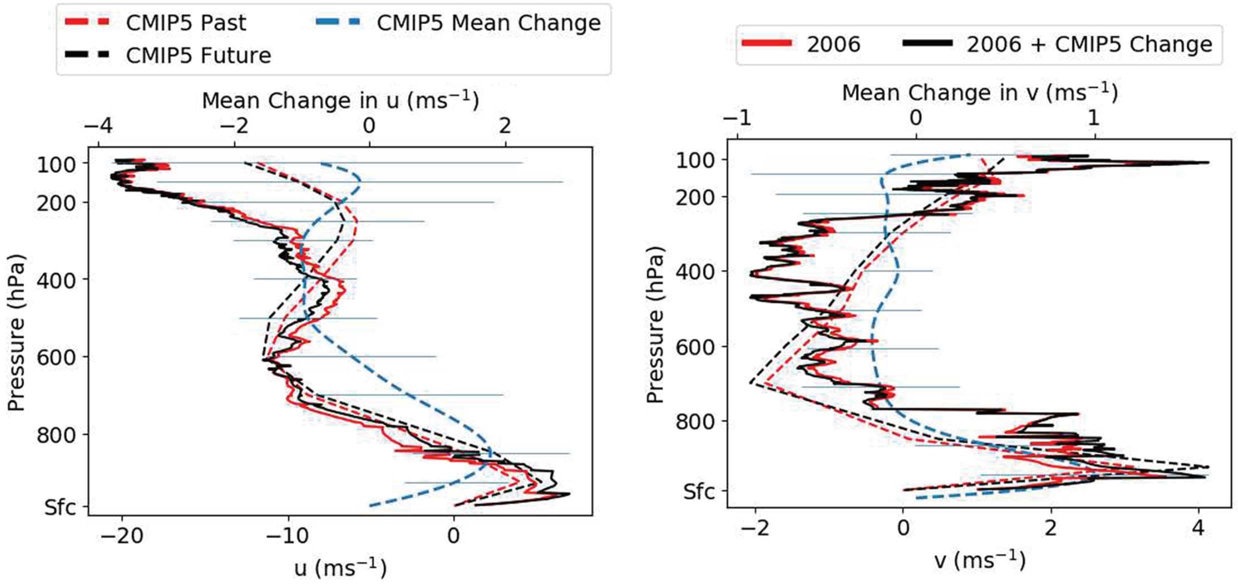

FIGURE 6 CMIP5 average across models of period 1950–1999 versus future (2070–2099) of u (westerlies) and v (southerlies) respectively (dashed). The AMMA control profile (red dotted) and the same with CMIP5 changes applied (black dotted). The mean interpolated change across models is also plotted with standard deviation shown

2.5.1 | Vertical velocities

Integrated CAPE (ICAPE) measures the latent heating per unit area accomplished collectively by all unstable parcels as they ascend from their level of free convection to their equilibrium level:

$$\mathrm{ICAPE} = \int_0^{z_{\mathrm{tr}}} \rho(z)\mathrm{CAPE}(z)\,\mathrm{d}z\,, \tag{1}$$

where CAPE(z) represents the CAPE of a parcel originating at z, while z_{tr} marks the height of the troposphere. A layer lifting index is then defined to measure the mean convective instability of the storm-relative inflowing tropospheric air by

$$\mathrm{CAPE}_{\mathrm{ll}} = \left(\int_0^{z_{\mathrm{tr}}} \rho(z)\,|u_{\mathrm{env}} - \mathrm{PS}|\,\mathrm{CAPE}(z)\,\mathrm{d}z\right) \times \left(\int_0^{z_{\mathrm{tr}}} \rho(z)\,|u_{\mathrm{env}} - \mathrm{PS}|\,\mathrm{d}z\right)^{-1}. \tag{2}$$

The propagation speed of the storm is defined as PS, while u_{env} is the environmental wind profile. Alfaro (2017) defines an index for updraught strength as

$$w_{\mathrm{ll}} = \sqrt{2\mathrm{CAPE}_{\mathrm{ll}}}. \tag{3}$$

2.5.2 | Precipitation

Alfaro and Khairoutdinov (2015) find that precipitable water is related to the surface precipitation rate. For constant low-tropospheric wind shear, the rate of water vapour processed by a squall line is the main factor affecting precipitation rate. However, Alfaro and Khairoutdinov (2015) also discuss that precipitation efficiency decreases with weaker shear, drier mid-tropospheric conditions and thus lower vertical velocities within the storm. The following equation (Alfaro, 2017) describes a diagnostic for the precipitation rate which depends on the factors discussed:

$$\mathrm{PR}_{\mathrm{ll}} = \left(\frac{w_{\mathrm{ll}}}{W}\right)^2 L_y \left(\int_0^{z_{\mathrm{tr}}} \rho q_v |u_{\mathrm{env}} - \mathrm{PS}|\,\mathrm{d}z\right), \tag{4}$$

where q_v is the WVMR and L_y is the length of the squall line in the along-line direction such that $\mathrm{PR}_{\mathrm{ll}}$ represents the total rainfall across the domain in kg·s^{-1}. The constant W should be selected such that the term $(\frac{w_{\mathrm{ll}}}{W})^2$ accounts for the efficiency of convection, the speed of upward-moving air, entrainment and the fraction of precipitable water that falls as precipitation. Thus, $\mathrm{PR}_{\mathrm{ll}}$ defines a diagnostic for the precipitation rate which depends on the water vapour inflow rate per unit length in the along-line direction.

The precipitation rate scaling in Equation 4 is expanded below and is proportional to the system-relative inflow of moist air and CAPE divided by the total system-relative inflow of total air mass:

$$\mathrm{PR}_{\mathrm{ll}} = \frac{2L_y\left(\int_0^{z_{\mathrm{tr}}} \rho\,|u_{\mathrm{env}} - \mathrm{PS}|\,q_v\,\mathrm{d}z\right) \times \left(\int_0^{z_{\mathrm{tr}}} \rho(z)\,|u_{\mathrm{env}} - \mathrm{PS}|\,\mathrm{CAPE}(z)\,\mathrm{d}z\right)}{W^2\left(\int_0^{z_{\mathrm{tr}}} \rho(z)\,|u_{\mathrm{env}} - \mathrm{PS}|\,\mathrm{d}z\right)}. \tag{5}$$

As $\mathrm{PR}_{\mathrm{ll}}$ describes the total rainfall rate for the domain, to convert this value into a mean rainfall rate in $\mathrm{mm{\cdot}hr^{-1}}$, it is necessary to divide by an area A. In this study we have divided by L_y and the y-averaged storm width (that is the y-width of rain rates greater than $1\ \mathrm{mm{\cdot}hr^{-1}}$).

3 | RESULTS

In this section, we first describe the control simulation and whether the squall line produced is consistent with observations of Sahelian MCSs during the WAM (Section 3.1). Once we have determined this, in Section 3.2 we then consider hypothesis 1 that recent increases in shear from both strengthened monsoon south-westerlies and the AEJ have increased the intensity of squall lines and hypothesis 2 that recent changes to the environmental thermodynamic profile may have influenced squall line intensity and may have been comparable to the effects of shear. Using the same set of simulations from profiles representative of wind and thermodynamic profiles from the 1980s and 2000s in Section 3.3, we test hypothesis 3 regarding whether the system-relative inflow of CAPE and water vapour is key to determining squall line updraught speeds and rainfall so that the LLMC can explain the modelled impacts of changing profiles. Finally, in 3.5, we consider hypothesis 4 that predicted future increases in shear, temperature and humidity will cause an increase in storm intensity.

3.1 | 2006 AMMA campaign control profile simulation

The simulation resulting from the control profile (Figure 1) is shown in Figure 7. The cold bubble results in two separate updraughts that can be seen to merge completely by hour 3. After this, the squall line begins to enter a more mature and steady state. The main convective updraught moves towards the front edge of the storm and appears to shrink slightly from around 20 to 10 km wide. The system speed is defined as the speed of the front edge of the cold pool moving at the front of the storm. A maximum surface pressure perturbation of 1.6 hPa occurs at around 4 hrs, which coincides with the squall line moving at its maximum speed and the main convective updraught jumping forward. The updraught appears to extend over the whole troposphere, and an overshoot can be seen at around 13 km while there is weak mesoscale ascent in the anvil. The anvil spreads out mainly westwards as a result of the strong Tropical Easterly Jet (around 100 hPa in Figure 1) to be hundreds of kilometres wide. There is an area of descending flow at the rear of the convective zone, but this appears to be moving at the same speed as the storm rather than providing a system-relative inflow. The area of precipitation of the storm spreads to about 80 km behind the front at 6 hrs and then shrinks slightly again.

We considered whether our simulated storm was consistent with those found in the West African Sahel. The control profile produced cold pools with an average propagation speed of $10.7\ \mathrm{m{\cdot}s^{-1}}$ across repeated experiments when in a steady state. This speed is consistent that of convective cloud clusters which have been found to propagate over the Sahel at $8\text{–}12\ \mathrm{m{\cdot}s^{-1}}$ (Mathon and Laurent, 2001). For composite Sahelian squall lines observed at Niamey in AMMA 2006, Provod *et al.* (2016) show mean rainfall rates between $10\ \mathrm{mm{\cdot}hr^{-1}}$ at the leading edge to $1\ \mathrm{mm{\cdot}hr^{-1}}$ at the trailing edge, with the storms taking on average an hour to pass. The mean rainfall rate of the storms simulated using the control profile is $7.2\ \mathrm{mm{\cdot}hr^{-1}}$, which is consistent with these measurements from 2006. Finally, the maximum surface pressure and minimum potential temperature perturbations for the control profile are 2.8 hPa and 6.8 °C, respectively, which are consistent with the storm composites of Provod *et al.* (2016) from the monsoon period, which show around 2 hPa and 6 °C for these quantities, respectively.

3.2 | Effects of past decadal changes in thermodynamics and shear from ECMWF ERA-Interim analyses

Simulations were run with thermodynamic and wind profiles produced by deducting recent decadal changes in ERA-Interim data from the 2006 control profile, to isolate the effect of recent thermodynamic changes from those within the wind profile and to test hypotheses 1 and 2. This allows for the comparison of four simulation configurations with two different thermodynamic environments, each with two wind profiles (Table 1). Maximum vertical velocities, $\overline{w}_{\max}$ and $\hat{w}_{\max}$, maximum rain rates $\hat{R}_{\max}$ and mean rain rates (where raining), $\overline{R}$, are described in Table 2 and plotted in Figure 8. All storms can be considered long lived and can be categorised as being in a steady state from 4 to 6.25 hrs. It appears as if the control case with 1980s winds begins to die after this point, and so times after 6.25 hrs were not considered.

In Figure 8, the thermodynamic change dominates the wind-shear change: the cases with 1980s thermodynamics (with higher CAPE and lower shear: red lines) have $\overline{w}_{\max}$ and $\overline{R}$ values of over $3\ \mathrm{m{\cdot}s^{-1}}$ and $5\ \mathrm{mm{\cdot}hr^{-1}}$ higher, respectively, than those with 2006 thermodynamics (i.e., with lower CAPE and higher shear: black lines). This supports hypothesis 2 that changes to the thermodynamic profile may have influenced squall-line intensity and could be comparable to the effects of shear. While

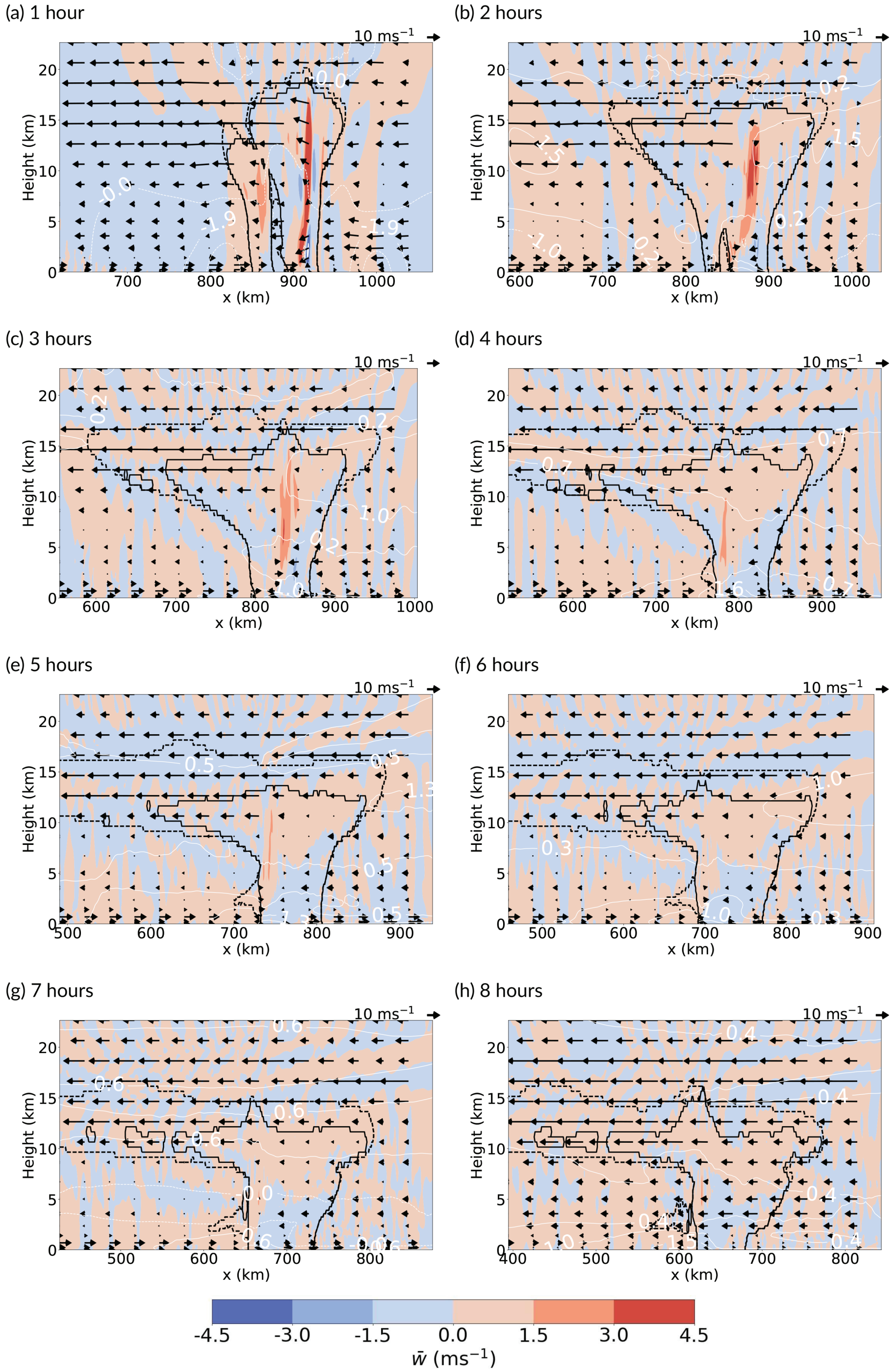

FIGURE 7 Simulation with the control profile from the 2006 AMMA campaign. A slice through the storm in the x–z plane is shown with y-averaged values shown (y-average is indicated by a bar, for example $\overline{w}$). Vertical velocity is shaded, pressure perturbation (hPa) in white contours, total liquid and solid water (dashed) and precipitation (solid) from 1 hr after initiation to 8 hrs in hourly intervals. The arrows represent $\bar{u}_r$-$\overline{w}$ where u_r are the system-relative wind speeds. Only (a) had vertical velocities higher than 4.5 m·s^{-1}, where the highest magnitude reached was 15.0

the impact of increasing wind shear for a constant thermodynamic profile (i.e., solid versus dashed lines) is less dramatic, it does result in higher rain rates and vertical velocities, approximately 2.5 mm·hr^{-1} and 0.5 m·s^{-1} respectively. This supports hypothesis 1 that stronger wind shear has strengthened the intensity of squall lines. The bulk indicators, $\overline{w}_{\max}$ and $\overline{R}$ (Table 2, Figure 8a,b) involve first averaging over the y domain and so lose the detail of extreme cases of velocity/rainfall in single convective cells. However, they tend to show more distinct differences between experiments. The difference in the noisier $\hat{w}_{\max}$ and $\hat{R}_{\max}$ (Table 2, Figures 8c–8d) is less obvious, as expected, but there is still an increase in $\hat{w}_{\max}$ with constant thermodynamic environments but increased wind shear. The standard error bars in Figure 8 show that the variation between the repeated experiments with different random seeds is less significant than the variations from different initial environments.

We next examine vertical cross-sections through the simulated squall lines (Figure 9) to provide a qualitative

TABLE 2 Diagnostics and variables

Variable	Description
ICAPE	From Alfaro (2017), the system-relative inflow of CAPE integrated over all z (Equation 1)
CAPE_{ll}	From Alfaro (2017), a diagnostic which describes the system-relative inflow of CAPE (Equation 2)
PR_{ll}	From Alfaro (2017), an indicator of precipitation rate (see Equation 4)
$\hat{w}_{\max}$	The maximum vertical velocity (in the x–z plane) averaged over (the along-squall-line) y-direction
$\overline{w}_{\max}$	The vertical velocity is averaged over the y domain (along the line of the storm). The maximum in the x–z plane of this average is then found
$w_{\max}$	The maximum value of vertical velocity across the entire domain
$\overline{R}$	Mean rain rate where raining. The mean value of all rain rates above a threshold of 1 mm·hr^{-1}
$\hat{R}_{\max}$	The maximum rain rate (in the x–z plane) averaged over (the along squall-line) y-direction

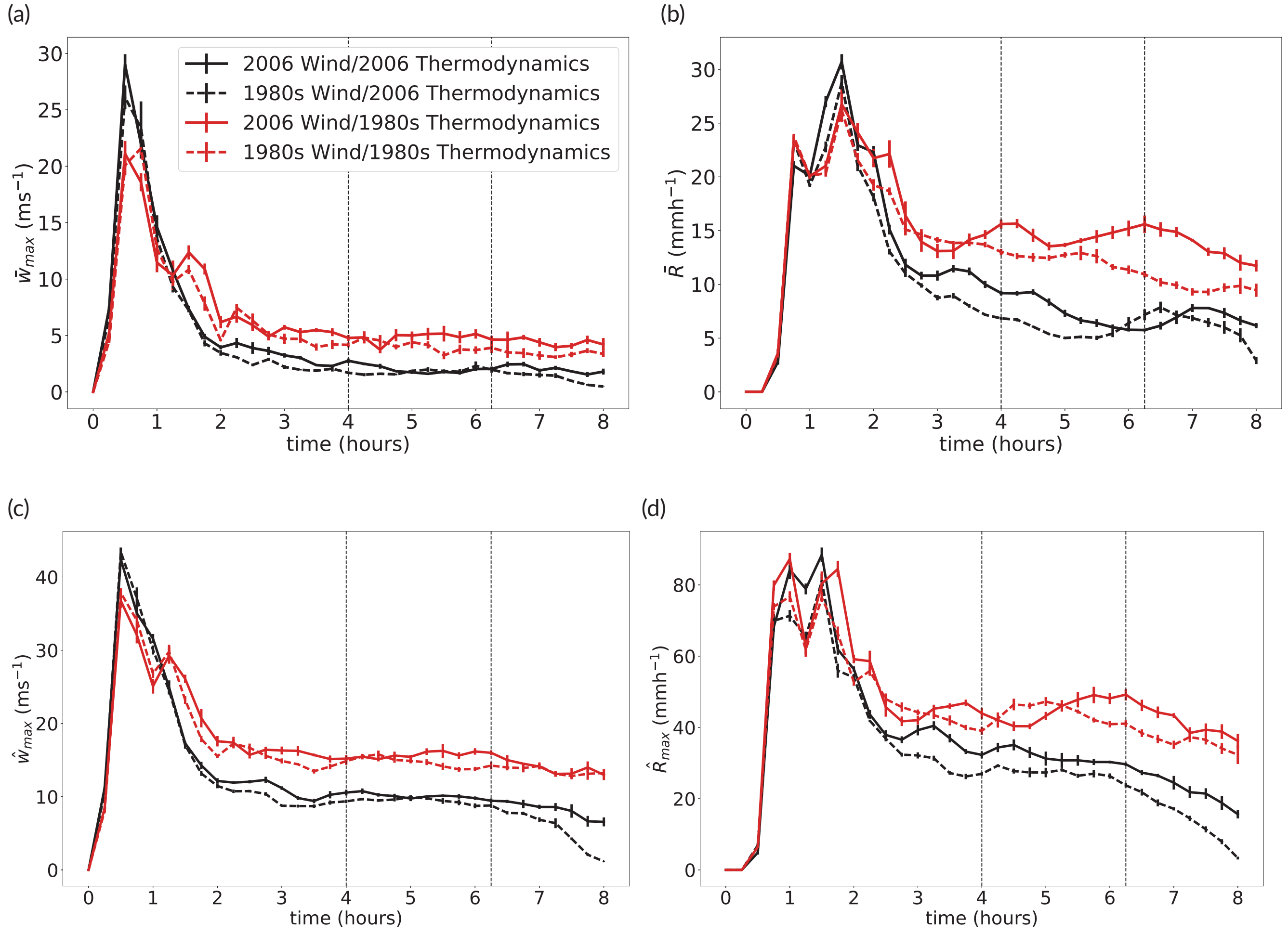

FIGURE 8 The top two figures show (a) the maximum vertical velocity and (b) the mean rain rate (where raining) in the y-averaged profile. See Table 2 for further descriptions of variables. The bottom figures show (c) y-averaged values of the maximum velocity, $\hat{w}_{\max}$ and (d) maximum rain rate, $\hat{R}_{\max}$ in the x–z plane. The mean of the five repeated experiments for each environmental profile is marked with the standard error of the mean shown by a vertical bar. This includes the control, control with ERA-Interim winds deducted, control with ERA-Interim thermodynamics deducted and control with both deducted. The dashed vertical lines indicate the period during which the storms are considered to be in a steady state from 4 to 6.25 hrs

examination of changes of squall-line structure as a function of the changes in thermodynamics and shear. All cases show squall lines with cold pools and a spreading anvil cloud to the west. The area usually associated with the rear inflow jet has downward movement with a horizontal velocity similar to that of the system. If the 2006 control thermodynamic cases (Figure 9a,b; lower CAPE/higher shear) are compared with the 1980s cases (Figure 9c,d; higher CAPE/lower shear), we see weaker updraughts, a wider precipitation area, a drier rear inflow jet (0.5–3 km), lower overshoots, a moister cold pool and a weaker meso-low ahead of the squall line. These differences are consistent with what we would expect for storms which occur in environments with lower CAPE.

3.3 | Testing the layer lifting model of convection

The LLMC, and thus hypothesis 3, was tested by plotting diagnostics w_{ll} and PR_{ll} against statistics calculated from the different simulations and time-averaged over the period when the storms were considered steady (Figure 10). The PS used was the speed of the cold pool for each storm averaged over the period when the MCS is considered to be in a steady state (from 4 to 6.25 hrs in the ERA-Interim experiments). The increased wind shear of the 2006 profile (circles versus squares) produces higher velocities, $\overline{w}_{\max}$ in Figure 10a, and rainfall, $\hat{R}_{\max}$ in Figure 10b; this change is small when compared with that from the thermodynamics (red versus black). The mean rain rate above a threshold of 1 mm·hr^{-1}, $\overline{R}$, consistently increases for higher wind shear across constant thermodynamic profiles (Figure 10c). However, the impact of changing wind shear on $\hat{R}_{\max}$ is less clear for the cases of constant 1980s thermodynamics (high CAPE). We suggest that $\hat{R}_{\max}$ is more thermodynamically controlled as it captures the rain rate of the most intense cumulonimbus cell, and thus less sensitive to MCS structure (and so to shear) than $\overline{R}$. The LLMC is therefore a useful indicator of vertical velocities and mean rainfall rates in these idealised experiments. This is particularly true for the bulk indicators of storm intensity.

The precipitation rate diagnostic, Equation 4, can not necessarily be universally used across thermodynamic profiles as the constant W may vary. We use a constant value of $W = 58.5$ m·s^{-1} for all cases, and despite this PR_{ll} is still a clear indicator of mean rainfall rates (Figure 10c). The value of W was chosen to fit the magnitude of PR_{ll} for the control profile experiments in Figure 10d to $\overline{R}$. The constant does not affect correlation, only the gradient of the best-fit line. PR_{ll} is also a useful indicator of storm intensity for cases of varied wind shear in a constant thermodynamic profile (circles versus squares). Furthermore, considering the linear relationship shown in Figure 10c, W can be concluded to be almost constant between these relatively similar environments. The average storm widths (where raining along y) were calculated for each individual storm (when considered steady). The width of raining area varied from 46 km for the higher shear/higher CAPE case to 70 km for the lower shear/lower CAPE case. These values were then used to calculate PR_{ll}/A in mm·hr^{-1}; Figure 10d displays how the diagnostic loses some skill through including this time-averaged value, with the correlation coefficient of the mean values falling from 0.98 to 0.97.

As discussed in Section 2, experiments were repeated to investigate the integrity of the results when changing the horizontal resolution. Figure 10a,c were reproduced for cases with horizontal resolution of both 200 m and 2 km. The gradient of the best-fit straight line in both cases was within 10% of that of the 1 km case, the LLMC continues to accurately predict the relative intensity of the storms, and the results support the conclusions made from our lower-resolution simulations. However, the vertical velocities were consistently slightly higher for the 200 m and lower for the 2 km resolution, consistent with the effects of the vertical velocity energy spectrum being better resolved. Interestingly, the gradient in both cases was steepest for the 200 m runs and least steep for the 2 km runs, suggesting that large grid spacings can decrease the modelled effects of shear, consistent with a lack of shear effects in the 4 km simulations used in Fitzpatrick *et al.* (2020) when compared with observations. Given the need to run long-duration large-domain convection-permitting simulations for future climate projections, this potential sensitivity merits future investigation.

The difference in cloud tops (maximum height reached by the cloud) can be viewed in the cross-sections shown in Figure 9. The 1980s (higher CAPE/lower shear) experiment in Figure 9d shows a higher overshoot, with a cloud top difference of 3 km, than the 2006 thermodynamics equivalent in Figure 9b (low CAPE/low shear). However, an increase in wind shear (from the 1980s to 2006) with the constant 1980s thermodynamics also results in a 1 km increase in cloud top height. This impact of increasing shear is representative of the results of Taylor *et al.* (2017), which have been corroborated by Fitzpatrick *et al.* (2020), whereby satellite data reveal growing numbers of clouds with colder cloud top temperatures and thus higher cloud top height over time, as shear increases.

PR_{ll} was expanded in Section 2.5 Equation 5, and the terms of interest are plotted in Figure 11. The first three figures explore the relative inflow of mass, CAPE and moisture at each height for the different environments.

(a) 2006 Wind / 2006 Thermodynamics

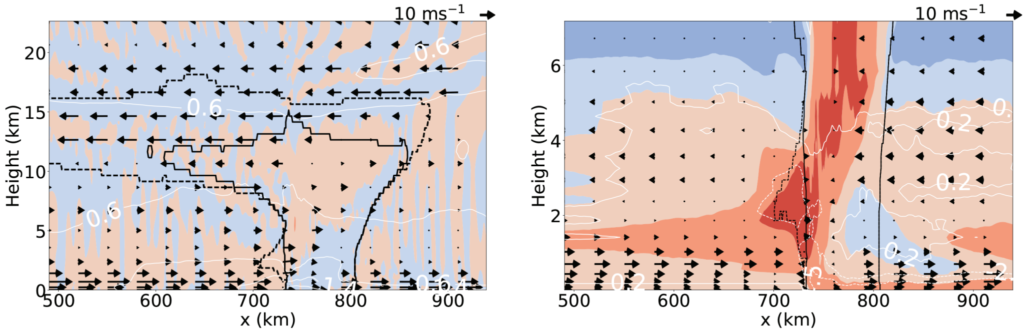

(b) 1980s Wind / 2006 Thermodynamics

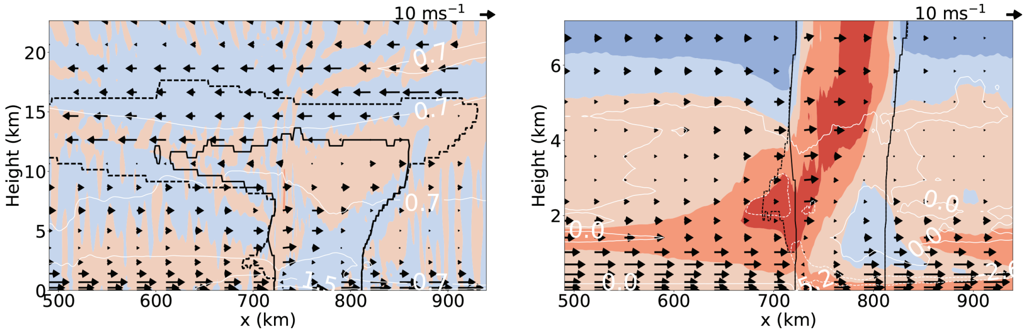

(c) 2006 Wind / 1980s Thermodynamics

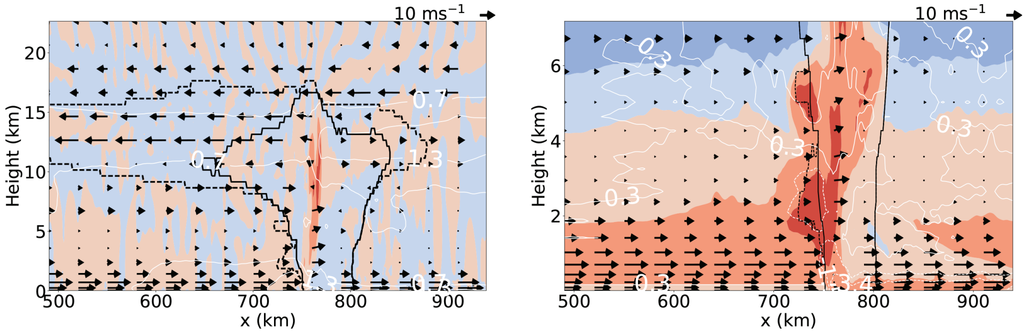

(d) 1980s Wind / 1980s Thermodynamics

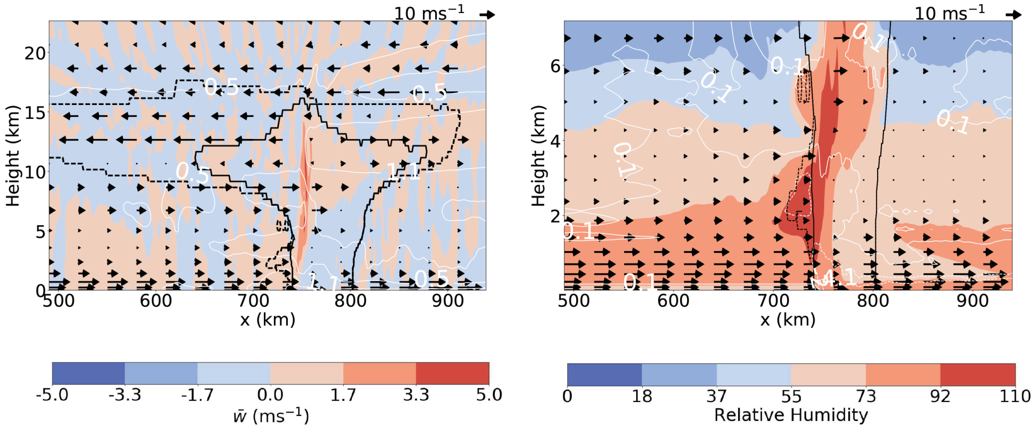

FIGURE 9 *y*-averaged values for the ECMWF ERA-I set of experiments shown at 5 hrs. Vertical velocities (left) and relative humidity (right) shown by shaded contours, total liquid and solid water content (dashed) and precipitation (solid black). White contours indicate perturbations from the original pressure profile. The arrows represent $\bar{u}_r$-$\overline{w}$, where u_r are the system-relative wind speeds

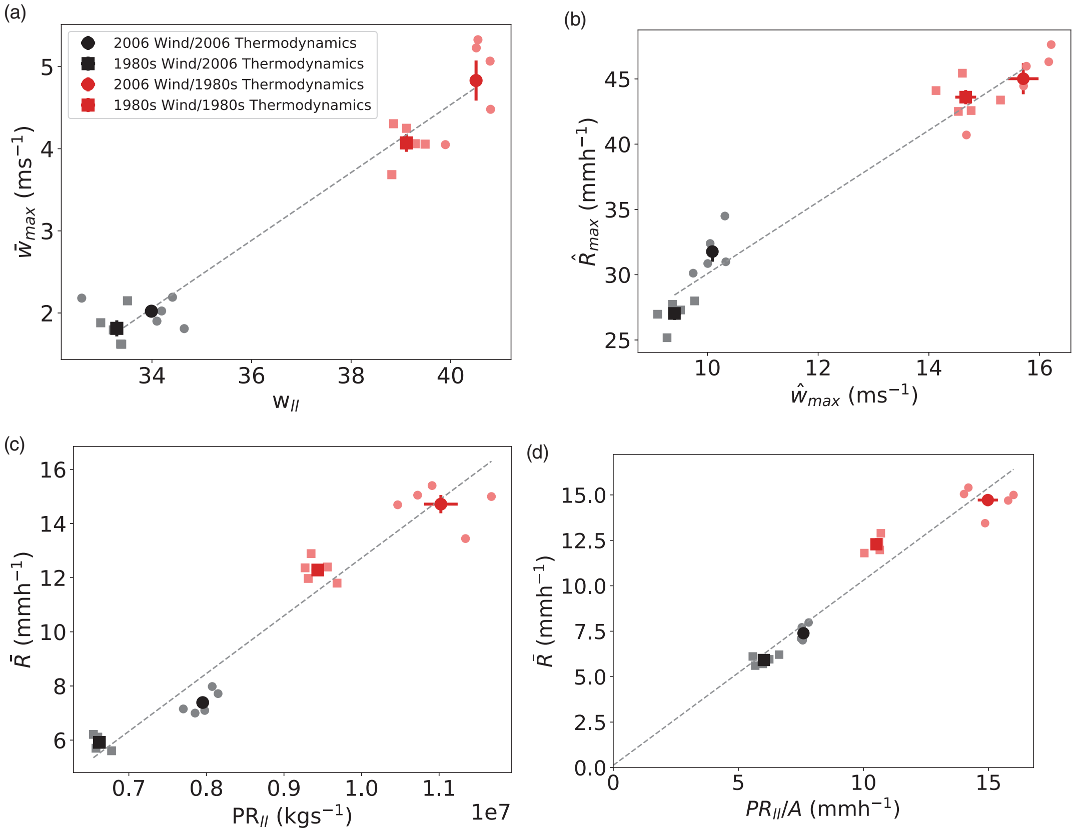

FIGURE 10 Time-averaged statistics for the duration the storms are steady in the ECMWF ERA-Interim experiments. The mean of the five repeated experiments for each environmental profile is marked with the standard error of the mean shown by a cross. (a) The index for updraught strength, $w_{\text{ll}} = \sqrt{\text{CAPE}_{\text{ll}}}$, plotted against $\overline{w}_{\text{max}}$, (b) $\overline{w}_{\text{max}}$ against $\overline{R}_{\text{max}}$, (c) the precipitation rate diagnostic PR_{ll} against the mean rain rate $\overline{R}$ and the same with (d) PR_{ll}/A, calculated through division by raining area width (where raining) for each individual case

The strong south-westerly nocturnal winds dominate for mass with a maximum inflow of 17.5 $\text{kg}\cdot\text{m}^{-2}\cdot\text{s}^{-1}$ in Figure 11a at 975 hPa and only begin to decrease at 925 hPa. This is also true for inflowing CAPE and moisture, both of which have secondary maxima at the low-level jet.

The higher CAPE near the surface in the 1980s thermodynamic cases results in maximum inflows of 10,000 $\text{J}\cdot\text{m}^{-2}\cdot\text{s}^{-1}$ higher than their equivalent 2006 wind profiles (red versus black in Figure 11b). Increasing the low-level winds for a constant thermodynamic profile (solid versus dashed lines) results in a smaller but still significant increase of inflowing CAPE. Above the near-surface maximum, the inflowing CAPE in Figure 11b then drops more dramatically than the mass in Figure 11a, which corresponds to a similar drop in CAPE at 920 hPa in Figure 2. The inflowing mass is a dominant factor here as it controls the fraction of convectively unstable air within the storm. As the fractional change in WVMR from the 1980s to 2000s is less substantial than that of the CAPE, the wind profile is more important for changes in the system-relative inflow of water (Figure 11c) than for CAPE (Figure 11b). In fact, for the system-relative inflow of water, the change in shear dominates the change in thermodynamics. However, lower values of specific and relative humidity at mid-levels in the 2006 profile could also be responsible for suppressing convection through entrainment. These processes are not directly captured by the LLMC.

To calculate the layer lifting indices such as CAPE_{ll} and PR_{ll}, the propagation speed of the MCS is required, and this is not predicted with the conceptual model of Alfaro (2017). Different choices for PS are considered and the resultant PR_{ll} plotted for each of the experiments against $\overline{R}$ as in Figure 10c (not shown). The different PS investigated included the speed of the storm when steady for each individual experiment, the average speed across repeated experiments with the same environment but unique small-scale random noise and the average across all experiments over all environments. The correlation coefficient was similar, approximately 0.98, for cases looking at the same environment and 0.97 for the average over all environments. To summarise, although environment-specific PS values result in more accurate

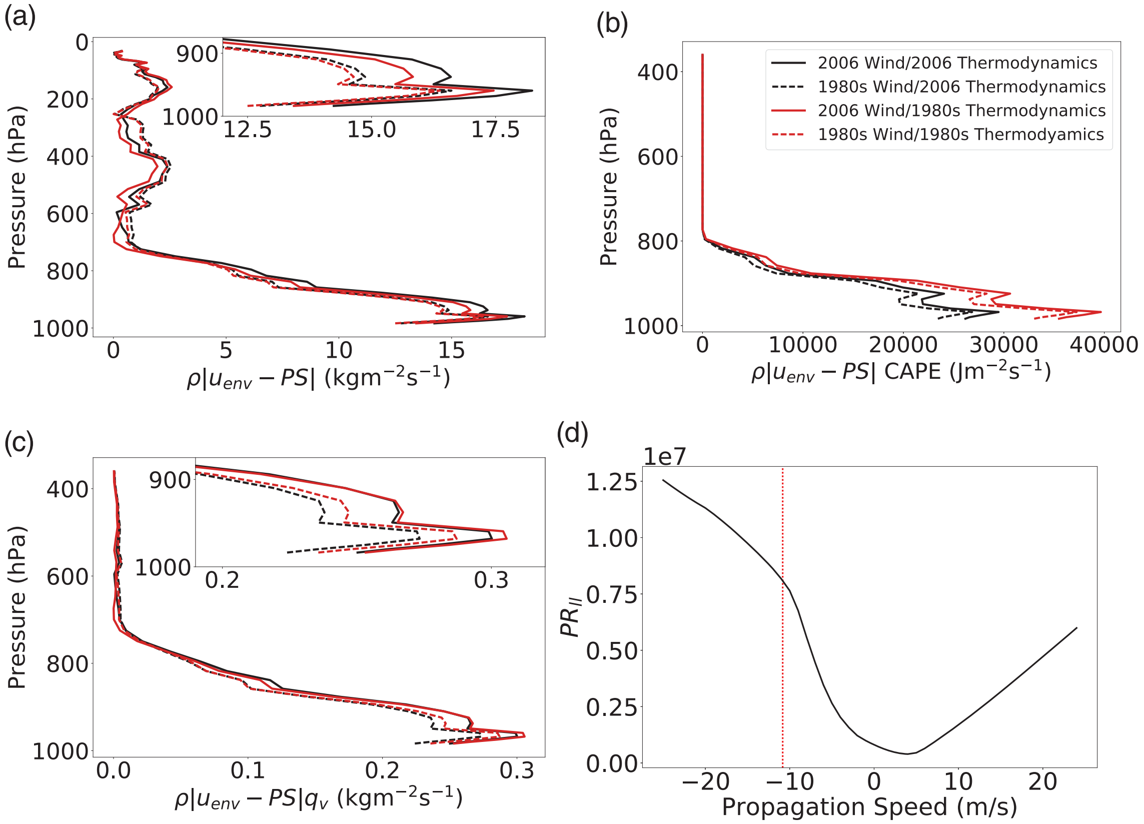

FIGURE 11 System relative inflows of: (a) mass, (b) CAPE and (c) water vapour at different heights for the different profiles. (d) Explores the relationship between the chosen propagation speed PS and the resultant $\mathrm{PR_{ll}}$ for the control profile. The red dotted line represents the mean speed of the control profile storm when it is in a steady state

values for $\mathrm{PR_{ll}}$, there is no stark change in results since variations in PS are small throughout our experiments where we simply modify one control profile.

Although the PS did not vary greatly in our experiments, it is not clear that this would hold in general as squall lines can travel both slower and faster than our experiments have shown (Barnes and Sieckman, 1984). Therefore, the sensitivity of $\mathrm{PR_{ll}}$ to PS in Equation 5 was further investigated in Figure 11d for the control run, where it is evident that an accurate value of PS is required. If the PS used is multiplied by a factor of 2 or 0.5, this results in the $\mathrm{PR_{ll}}$ being out by a factor of 1.5 and 0.3, respectively. If PS is set to zero, the PR_{ll} is 1/11 of the original value. This complicates the process of parametrising convection as the resultant rainfall of the storm is a function of not only the environmental thermodynamics but also storm motion, which may be a function of storm dynamics as well as the profile.

The line plot in Figure 11d is somewhat artificial as not all propagation speeds are realistic for this profile. Figure 12 more fully explores sensitivities to shear and propagation speed within the layer lifting model. The shear has been varied by multiplying the entire wind profile by factors of 0.5 to 1.5, and the resultant magnitude of the AEJ is plotted on the *y*-axis of the figure. The sensitivity of rainfall to shear is much lower than the sensitivity to propagation speed. Overall Figure 12 suggests that, theoretically, we expect shear to increase rain, consistent with Taylor *et al.* (2017), unless the PS barely increases with shear, in which case the quantity of air entering the storm from above the LFC (Figure 2) will increase at a greater rate as $|u_{\mathrm{env}} - \mathrm{PS}|$ will no longer be near zero at the AEJ. More air from above the LFC results in a reduction in the total fraction of convectively unstable air entering the storm. However, Taylor *et al.* (2017) showed that systems with colder cloud top temperatures (i.e. of higher intensity) were indeed associated with significant increases in PS. Whether a faster system facilitates increased storm intensity or is a consequence of it is unclear, but fundamentally PS and system intensity are coupled. The solid line in Figure 12 marks the AEJ as the steering level of the storm (e.g. the PS is equal to the maximum of the AEJ), which is supported by the black markers (indicating the PS of our experiments with the control wind profile). If the AEJ does control the PS of storms, then an increase in the AEJ could result in more rainfall and a correlating increase in shear. Although the model appears to support the hypothesis that shear has increased storm intensity, it is worth noting that,

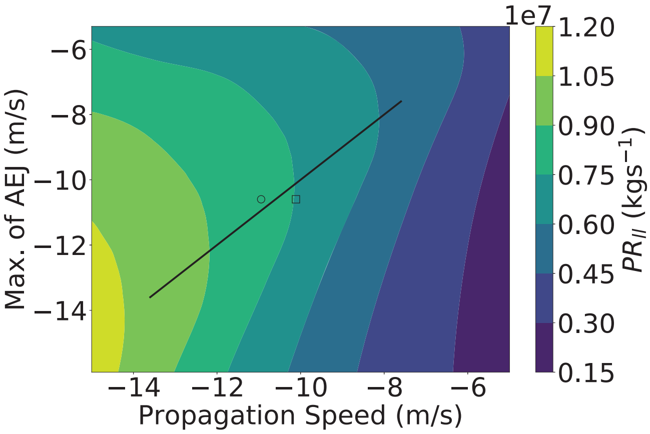

FIGURE 12 Sensitivity test of Equation 4 for propagation speed versus shear using the 2006 temperature and humidity profiles. For each case, the environmental wind profile has been multiplied by a factor so that, although only the value of the AEJ is shown, the nocturnal jet has also been increased. The black line indicates where the AEJ maximum is equal to the propagation speed. The experiments with the 2006 wind profile are plotted: control (circle) and ECMWF thermodynamics (square)

in a potential scenario with a strengthening LLJ but constant shear (weakening AEJ), the fraction of moisture and convectively unstable air entering the storm would also increase.

In conclusion, we quantified the effects of plausible past decadal changes in humidity and shear, to test our hypothesis 1 that increased shear may have increased severe storms in the Sahel over the period from 1982 to 2017, while also testing hypothesis 3 regarding whether the LLMC can explain the modelled impacts of changing environmental profiles through calculating the system-relative inflow of CAPE and water vapour. We cannot reject either hypothesis, and increased shear is seen to increase both measures of convective intensity (i.e. updraughts and rainfall), although for the changes used temperature and humidity changes are the dominant drivers of the total rainfall changes. Given the innate variability across the Sahel region, including on a daily scale, understanding the potential effects caused by these changes in wind profile and thermodynamics is enlightening.

3.4 | Uncertainty in past trends from reanalyses

Section 3.2 shows how stronger shear increases storm vertical velocities and rainfall, consistent with Alfaro (2017) and supporting the conclusions of Taylor *et al.* (2017). However, the results of a decrease in storm intensity from the 1980s profile to the 2006 control profile do not reflect the increase in storm intensity discussed in Taylor *et al.* (2017), likely due to our decrease in the WVMR with time at low and mid-levels, which results in our 1980s profile having higher CAPE and lower CIN than our 2006 profile.

Considering the sparsity of weather stations and radiosondes which regularly measure atmospheric conditions across the African continent, it is necessary to view reanalysis such as ERA-Interim for these regions with caution (Roberts *et al.*, 2015). Additionally, changes in satellite observation systems may have adversely affected the ECMWF reanalyses, making trend analysis difficult. This is particularly true for temperature and humidity in the tropics (Trenberth *et al.*, 2001). To gain some perspective, data from The Modern-Era Retrospective analysis for Research and Applications version 2 (MERRA-2) for the months of June to September at all times across 15 °E–15 °W and 16–17 °N were compared with ECMWF ERA-Interim and ECMWF ERA-5 analyses for the same region. On a direct comparison of variables at set heights, it can be seen that, not only do the three reanalyses disagree on mean values, but they also give different magnitudes and indeed signs in trends over time. For instance, Figure 13a shows similar values for specific humidity at 850 hPa in all models after the year 2000, but the higher values of 0.011 kg·kg^{-1} in ERA-Interim compared with 0.009 kg·kg^{-1} in MERRA-2 at the start of 1990s and particularly the low of 0.008 kg·kg^{-1} in ERA-5 ensure a slight increasing trend in humidity in MERRA-2, a somewhat more significant one in ERA-5 and a decrease in ERA-Interim. Similarly, ERA-Interim and MERRA-2 show slight increases in temperature at 850 hPa in Figure 13b, while ERA-5 remains fairly constant. It is the trend in thermodynamics that dominates our results in Section 3.2, but significantly these trends, taken from reanalyses, are uncertain. Figure 3 reveals large spatial variability in WVMR over the region we have averaged over, which creates added complexity. Although decadal trends for the region could be obtained directly from radiosondes, we do not pursue this as it is unclear how representative that would be. Humidity measurements are sensitive to the type of radiosonde used (as seen in the spurious diurnal cycle in AMMA sondes Agustí-Panareda *et al.*, 2009). Additionally, observations would be from a single location. Taylor *et al.* (2017) considered what trends could be inferred from different collections of radiosonde observations from across the Sahel region and summarised them to be a warming of the SAL relative to the underlying Sahelian PBL and increased easterlies at 700 hPa, since the 1980s.

The trends in wind speeds can also be compared between reanalyses. The magnitude of the AEJ increases at 600 hPa by approximately 1.5 m·s^{-1} for ERA-5 and MERRA-2 while remaining fairly constant for

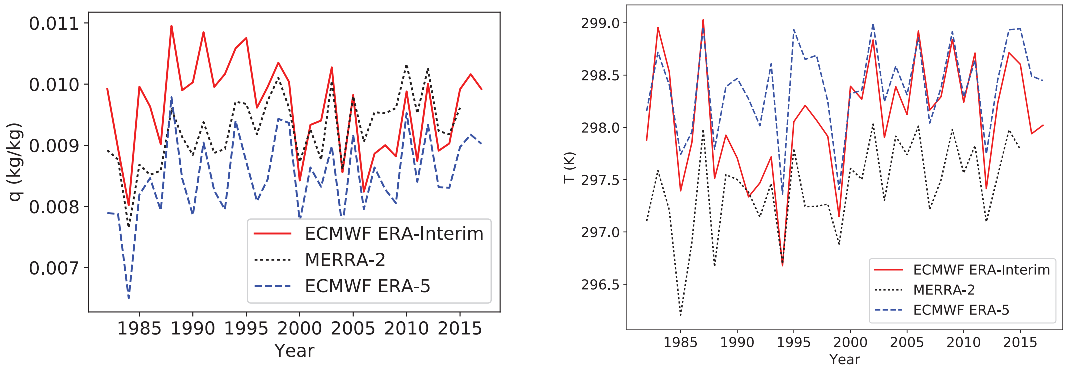

(a) Specific Humidity at 850hPa

(b) Temperature at 850hPa

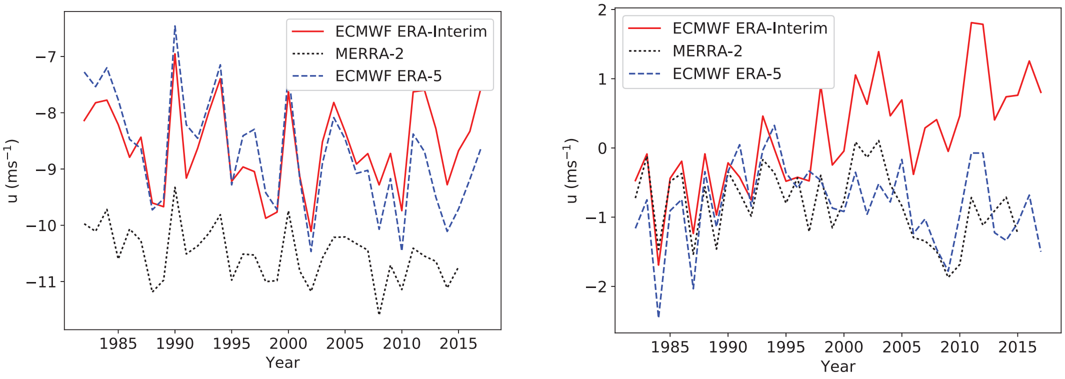

(c) Westerlies at 600hPa

(d) Westerlies at 850hPa

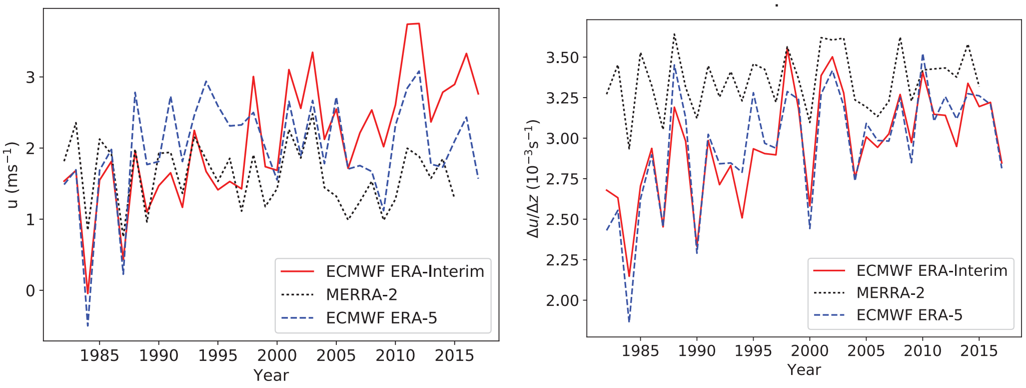

(e) Westerlies at 925hPa

(f) Westerlies Wind Shear (925 -600hPa)

FIGURE 13 Comparison of mean annual values from 1982 to 2017 of ECMWF ERA-Interim data against MERRA-2 and ECMWF ERA-5 reanalysis for June to September monthly averages for the region 15 °W-15 °E and 16 °–17 °N (all times of the day included)

ERA-Interim (Figure 13c). The lack of a marked increase in westerlies at both 850 hPa (Figure 13d) and 925 hPa (Figure 13e) in MERRA-2 and ERA-5 is also notable compared with ERA-Interim. When the wind shear is compared in Figure 13f however, despite the disparities between wind speeds at different heights between the two ECMWF cases, the shear increase is similar compared with the fairly constant shear in MERRA-2. These differences highlight that the uncertainty in past trends in both thermodynamics and shear is large enough that it may change their relative roles for storm trends.

3.5 | Implications for future rainfall

The previous sections have shown that shear changes can drive intensification of rainfall. Under climate change, warming allows for higher WVMR, leading to increased

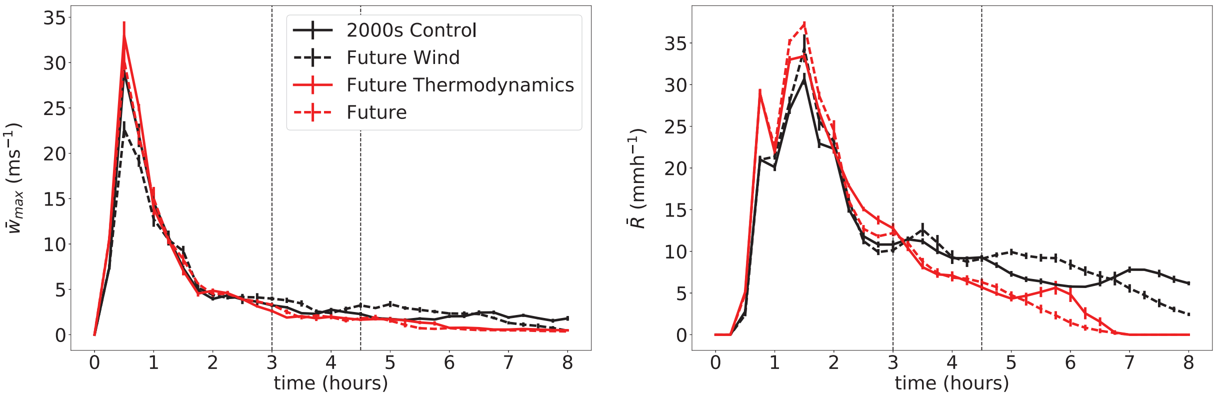

FIGURE 14 Maximum *y*-averaged (bulk measure) of vertical velocity and the mean rain rate (where raining). Mean values are plotted, and the error bars mark the standard error of the mean for all CMIP5 experiments including the control, control with CMIP5 winds applied, control with CMIP5 thermodynamics applied and control with both applied. The dashed vertical lines indicate where the storms are considered to be in a steady state

rain rates (Kendon *et al.*, 2019). The Sahara is expected to continue to warm faster than the Gulf of Guinea under climate change (Dong and Sutton, 2015), which is expected to increase shear. It is important to question the extent to which such changes in shear may affect future Sahelian MCSs, alongside effects from the change in the thermodynamic profile. Given the success of the LLMC indices in Section 3.2, we investigate the possible role of shear changes versus thermodynamic changes under climate change.

Figure 14 shows that the future climate thermodynamic change imposed dominates the shear change imposed. When compared with the current climate thermodynamic profile (black), the future thermodynamic profile (red) results in higher bulk measures of vertical velocities and rainfall in the spin-up, but the storm does not remain sustained for as long and dies off earlier. This results in a shorter period during which the storms can be considered as “steady”. During the period of 3–4.5 hrs which has been marked, the future thermodynamic storms (red) are “dying” and thus the vertical velocities and rain rate are lower than for the current period.

A time progression of vertical cross-sections of the experiments is shown in Figure 15. Again, all cases show squall lines with cold pools and anvil clouds spreading to the west. In the 2006 control case (lower CIN/lower CAPE/lower shear) compared with the future (higher CIN/higher CAPE/higher shear), we see: stronger updraughts, a drier rear inflow jet (0.5–3 km), drier cold pool and a weaker meso-low ahead of the squall line. The difference in CIN explains these variations, in that after the spin-up the lower CIN in the control 2006 profile allows a more sustained storm.

Figure 14 shows that increased wind shear (dashed lines) produces an increase in vertical velocities and rain for the control run thermodynamics; this is only seen for rain in the future thermodynamic experiments, and here it is smaller and more short lived (consistent with the earlier demonstrated greater role of shear for the system-relative inflow of water than for the system-relative inflow of CAPE). In both thermodynamic environments, the future wind profile causes the storms to die earlier. Similarly to our analysis of experiments investigating recent ERA-Interim trends in Section 3.2, the thermodynamic changes dominate compared with applied environmental wind changes, although the effects of shear can still be seen. It is also worth noting that, although the ERA-Interim experiments are longer lived than the future climate cases, the control with ERA-Interim wind case begins to die out after 6.25 hrs and thus does not sustain for that much longer.

4 | CONCLUSIONS

Previous studies have suggested that increased shear in the Sahel has caused a recent intensification of Sahelian squall lines (Taylor *et al.*, 2017) while predicting that a warming Sahara (through climate change) will result in stronger wind shear over the Sahel (Dong and Sutton, 2015). To investigate the suggested role of shear for past and future change, we analysed idealised LES of squall lines in an environmental setting representative of night conditions in the Sahel during the West African Monsoon. Initial profiles were based on soundings from the 2006 AMMA campaign observations made at Niamey. This control profile was then modified using environmental thermodynamic and wind profile changes calculated from ERA-Interim data for the period of 1982–2017, giving a 1980s profile with decreased shear, increased CAPE and decreased CIN

FIGURE 15 y-averaged values for the CMIP5 experiments shown at 3 hrs: relative humidity (shaded contours), total liquid and solid water content (dashed black) and precipitation (solid black). White contours indicate perturbations from the original pressure profile. The arrows represent $\bar{u}_{\mathrm{r}}$-$\overline{w}$, where u_{r} are the system-relative wind speeds

(a) Past Wind / Past Thermodynamics

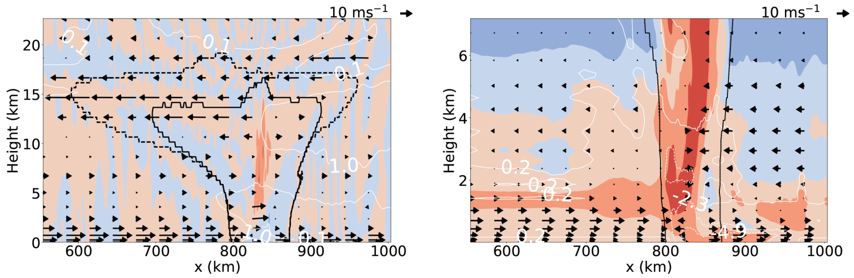

(b) Future Wind / Past Thermodynamics

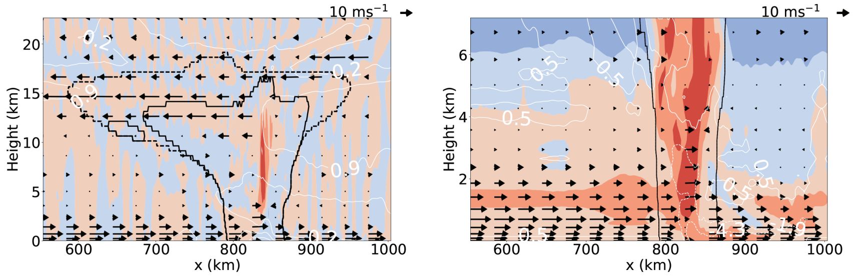

(c) Past Wind / Future Thermodynamics

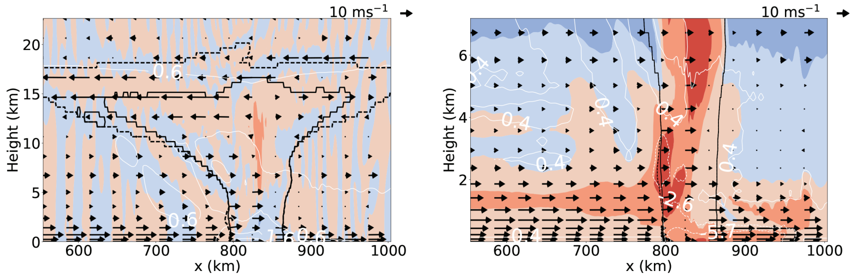

(d) Future Wind / Future Thermodynamics

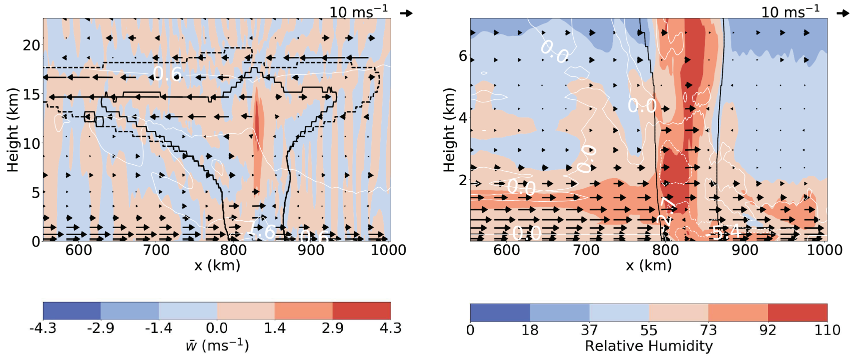

when compared with the control 2006 environment. Additionally, the profile was also modified with long-term predictions from CMIP5 for the Niamey region. The CMIP5 mean predicts increased low-level south-westerly winds, a stronger AEJ whose maximum extends higher than currently and an increase in both CAPE and CIN.

In the idealised experiments, for constant thermodynamic profiles, the increased wind shear of the 2006 control caused greater values of storm vertical velocities and rainfall, which supports our hypothesis 1 that recent increases in shear from both strengthened monsoon south-westerlies and the AEJ caused by Saharan warming have increased the intensity of squall lines. However, in our simulations, the effects of the thermodynamic changes imposed dominated the effects of the shear changes imposed: for the 1980s cases, the higher CAPE and lower CIN resulted in higher vertical velocities and mean rainfall. Comparison of the ERA-Interim, MERRA-2 and ERA-5 showed that there were significant differences between the three datasets, including in the signs of decadal trends in both humidity and shear (although shear tends to increase). Our results, therefore, support the conclusions made in Taylor *et al.* (2017) that increased wind shear could be the main driver of decadal changes in storm intensity in the Sahel. Our results also do not allow us to reject our hypothesis 2, that recent changes to the environmental thermodynamic profile may have influenced squall line intensity and could be comparable to the effects of shear, but we note that an increase in humidity might be expected to increase moderate and severe storms, whereas shear is more compatible with the increase in severe but not moderate storms seen in Taylor *et al.* (2017). We conclude that quantifying the past thermodynamic change is vital to understanding past trends in squall line intensity. This highlights the need for an improvement in measurements for the region.

The LLMC (Alfaro, 2017) including indices for vertical winds and rain was tested to gain an understanding of changes in shear and thermodynamics. It was found that the diagnostics of Alfaro (2017) were an excellent indicator of squall line average ascent and rain rate, with maximum ascents and rain rates less well predicted, as expected. This agreement with the theory is an indicator that rainfall and heating in mature squall lines are primarily determined by the system-relative inflow of the environmental air, consistent with our hypothesis 3 that the LLMC can explain the modelled impacts of changing environmental profiles. The relative inflow of mass, CAPE and moisture for each of the environments were considered at different heights. The maximum inflow of all the properties entered the storms with the low-level jet, showing the importance of the jet for Sahelian MCSs. The precipitation rate diagnostic was found to be dependent on the propagation speed of the storm, which is not predicted in the model presented in Alfaro (2017). This suggests that using the environmental thermodynamic profile alone to parametrise convective events is problematic since the resultant rainfall of the storm is also a function of the storm's motion, and so internal dynamics and wind speeds, and that to predict storm intensity we have to be able to also predict storm speed. Finally, the accuracy of the LLMC raises questions over whether increases in storm intensity are correlated with stronger shear or the congruent increase in the low-level jet.

Simulations perturbed with the future thermodynamics predicted by CMIP5 models resulted in shorter-lived squall lines. This is consistent with the increase in CIN predicted across the CMIP5 models and accordant with large-domain convection-permitting future climate simulations (Kendon *et al.*, 2019; Fitzpatrick *et al.*, 2020). These short-lived storms suggest that large-scale convergence and synoptic variability may play an important role for storms in a future climate, and more work is needed to understand this relationship. Similar to the ERA-Interim experiments, the thermodynamic changes dominated the wind shear changes. Increased wind shear did increase rain, however, but also caused storms to die earlier for both thermodynamic profiles. It is important to note that there are large disparities across the different CMIP5 model predictions, not only in the magnitude of future changes, including wind shear, but whether they will be negative or positive. However, positive feedback between changes in temperature and water vapour are generally expected to enhance the Saharan heat low and so increase shear (Dong and Sutton, 2015; Evan *et al.*, 2015), which is consistent with our hypothesis 4 that predicted future increases in shear, temperature and humidity will cause an increase in storm intensity.

Finally, we note that our simulations are idealised situations and so ignore influences such as large-scale convergence, variations in the synoptic state, and the diurnal cycle including surface fluxes and radiation. Thus, further study is required on testing the layer-lifting scalings in less idealised settings, to more fully understand squall-line dynamics, and controls on past and future trends in squall line properties.

ACKNOWLEDGEMENTS

Thanks are due to Stephen Griffiths for his valuable input. We thank George Bryan for making the CM1 model freely available (https://www2.mmm.ucar.edu/people/bryan/cm1/). This work also relied on efforts by others including radiosonde data generated by the AMMA field campaign (Parker *et al.*, 2008), CMIP5 multi-model ensemble datasets (Taylor *et al.*, 2012), the European Centre for Mid-Range Weather Forecasts (ECMWF) reanalyses (Berrisford *et al.* 2011) and NASA's MERRA reanalyses (Rienecker *et al.*, 2011). This work was undertaken on ARC2 and ARC3, part of the High Performance Computing facilities at the University of Leeds, UK. Finally, we would like to thank our anonymous reviewers, whose revisions have improved the clarity and structure of our study.

ORCID

Megan E. Bickle https://orcid.org/0000-0003-4940-4738
Andrew N. Ross https://orcid.org/0000-0002-8631-3512
Douglas J. Parker https://orcid.org/0000-0003-2335-8198
Christopher M. Taylor https://orcid.org/0000-0002-0120-3198

REFERENCES

Agustí-Panareda, A., Vasiljevic, D., Beljaars, A., Bock, O., Guichard, F., Nuret, M., Garcia Mendez, A., Andersson, E., Bechtold, P., Fink, A., Hersbach, H., Jean-Philippe, L., Jean-Blaise, N., Parker, D.J., Jean-Luc, R. and Tompkins, A.M. (2009) Radiosonde humidity bias correction over the West African region for the special AMMA reanalysis at ECMWF. *Quarterly Journal of the Royal Meteorological Society*, 135(640), 595-617. http://dx.doi.org/10.1002/qj.396.

Alfaro, D.A. (2017) Low-tropospheric shear in the structure of squall lines: impacts on latent heating under layer-lifting ascent. *Journal of the Atmospheric Sciences*, 74, 229–248.

Alfaro, D.A. and Khairoutdinov, M. (2015) Thermodynamic constraints on the morphology of simulated midlatitude squall lines. *Journal of the Atmospheric Sciences*, 72, 3116–3137.

Barnes, G. and Sieckman, K. (1984) The environment of fast-and slow-moving tropical mesoscale convective cloud lines. *Monthly Weather Review*, 112, 1782–1794.

Berrisford, P., Dee, D., Poli, P., Brugge, R., Fielding, K., Fuentes, M., Kallberg, P., Kobayashi, S., Uppala, S. and Simmons, A. (2011) *The ERA-interim archive, version 2.0*. Technical Report.

Birch, C.E., Parker, D.J., Marsham, J.H., Copsey, D. and Garcia-Carreras, L. (2014) A seamless assessment of the role of convection in the water cycle of the West African Monsoon. *Journal of Geophysical Research: Atmospheres*, 119, 2890–2912.

Brown, R.G. and Zhang, C. (1997) Variability of midtropospheric moisture and its effect on cloud-top height distribution during TOGA COARE. *Journal of the Atmospheric Sciences*, 54, 2760–2774.

Browning, K.A. and Ludlam, F. (1962) Airflow in convective storms. *Quarterly Journal of the Royal Meteorological Society*, 88, 117–135.

Bryan, G.H. and Fritsch, J.M. (2002) A benchmark simulation for moist nonhydrostatic numerical models. *Monthly Weather Review*, 130, 2917–2928.

Bryan, G.H., Knievel, J.C. and Parker, M.D. (2006) A multimodel assessment of RKW theory's relevance to squall-line characteristics. *Monthly Weather Review*, 134, 2772–2792.

Bryan, G.H. and Morrison, H. (2012) Sensitivity of a simulated squall line to horizontal resolution and parameterization of microphysics. *Monthly Weather Review*, 140, 202–225.

Bryan, G.H., Wyngaard, J.C. and Fritsch, J.M. (2003) Resolution requirements for the simulation of deep moist convection. *Monthly Weather Review*, 131, 2394–2416.

Burpee, R.W. (1972) The origin and structure of easterly waves in the lower troposphere of North Africa. *Journal of the Atmospheric Sciences*, 29, 77–90.

Dong, B. and Sutton, R. (2015) Dominant role of greenhouse-gas forcing in the recovery of Sahel rainfall. *Nature Climate Change*, 5, 757–760.

Durran, D.R. and Klemp, J.B. (1983) A compressible model for the simulation of moist mountain waves. *Monthly Weather Review*, 111, 2341–2361.

Evan, A.T., Flamant, C., Lavaysse, C., Kocha, C. and Saci, A. (2015) Water vapor forced greenhouse warming over the Sahara Desert and the recent recovery from the Sahelian drought. *Journal of Climate*, 28, 108–123.

Fink, A.H. and Reiner, A. (2003) Spatiotemporal variability of the relation between African easterly waves and West African squall lines in 1998 and 1999. *Journal of Geophysical Research: Atmospheres*, 108.

Fitzpatrick Rory, G.J., Parker Douglas, J., Marsham John, H., Rowell David, P., Guichard Francoise, M., Taylor Chris, M., Cook Kerry, H., Vizy Edward, K., Jackson, L.S., Finney, D., Crook, J., Stratton, R. and Tucker, S. (2020) What Drives the Intensification of Mesoscale Convective Systems over the West African Sahel under Climate Change?. *Journal of Climate*, 33(8), 3151–3172. http://dx.doi.org/10.1175/jcli-d-19-0380.1.

Fovell, R.G. and Tan, P.-H. (1998) The temporal behavior of numerically simulated multicell-type storms. Part II: the convective cell life cycle and cell regeneration. *Monthly Weather Review*, 126, 551–577.

Garcia-Carreras, L., Marsham, J.H., Parker, D.J., Bain, C., Milton, S., Saci, A., Salah-Ferroudj, M., Ouchene, B. and Washington, R. (2013) The impact of convective cold pool outflows on model biases in the Sahara. *Geophysical Research Letters*, 40, 1647–1652.

Gilmore, M.S. and Wicker, L.J. (1998) The influence of midtropospheric dryness on supercell morphology and evolution. *Monthly Weather Review*, 126, 943–958.

James, R.P. and Markowski, P.M. (2010) A numerical investigation of the effects of dry air aloft on deep convection. *Monthly Weather Review*, 138, 140–161.

Kendon, E.J., Stratton, R.A., Tucker, S., Marsham, J.H., Berthou, S., Rowell, D.P. and Senior, C.A. (2019) Enhanced future changes in wet and dry extremes over Africa at convection-permitting scale. *Nature Communications*, 10, 1–14.

Klein, C., Nkrumah, F., Taylor, C.M. and Adefisan, E.A. (2021) Seasonality and Trends of Drivers of Mesoscale Convective Systems in Southern West Africa. *Journal of Climate*, 34(1), 71–87. http://dx.doi.org/10.1175/jcli-d-20-0194.1.

Kniffka, A., Knippertz, P., Fink, A.H., Benedetti, A., Brooks, M.E., Hill, P.G., Maranan, M., Pante, G. and Vogel, B. (2020) An evaluation of operational and research weather forecasts for southern West Africa using observations from the DACCIWA field campaign in June–July 2016. *Quarterly Journal of the Royal Meteorological Society*, 146, 1121–1148.

Lavaysse, C., Flamant, C., Janicot, S., Parker, D.J., Lafore, J.-P., Sultan, B. and Pelon, J. (2009) Seasonal evolution of the West African heat low: a climatological perspective. *Climate Dynamics*, 33, 313–330.

Lebel, T., Diedhiou, A. and Laurent, H. (2003) Seasonal cycle and interannual variability of the Sahelian rainfall at hydrological scales. *Journal of Geophysical Research: Atmospheres*, 108.

Lebel, T., Parker, D.J., Flamant, C., Bourlis, B., Marticorena, B., Mougin, E., Peugeot, C., Diedhiou, A., Haywood, J.M., Ngamini, J.B., Polcher, J., Redelsperger, J.-L. and Thorncroft, C.D. (2010) The AMMA field campaigns: multiscale and multidisciplinary observations in the West African region. *Quarterly Journal of the Royal Meteorological Society*, 136(S1), 8–33. http://dx.doi.org/10.1002/qj.486.

Lebo, Z. and Morrison, H. (2015) Effects of horizontal and vertical grid spacing on mixing in simulated squall lines and implications for convective strength and structure. *Monthly Weather Review*, 143, 4355–4375.

Ludlam, F. (1963). Severe local storms: a review, *Severe Local Storms*, Springer, pp. 1–32.

Marsham, J.H., Dixon, N.S., Garcia-Carreras, L., Lister, G., Parker, D.J., Knippertz, P. and Birch, C.E. (2013) The role of moist convection in the West African monsoon system: insights from continental-scale convection-permitting simulations. *Geophysical Research Letters*, 40, 1843–1849.

Mathon, V. and Laurent, H. (2001) Life cycle of sahelian mesoscale convective cloud systems. *Quarterly Journal of the Royal Meteorological Society*, 127, 377–406.

Morrison, H., Curry, J. and Khvorostyanov, V. (2005) A new double-moment microphysics parameterization for application in cloud and climate models. Part I: description. *Journal of the Atmospheric Sciences*, 62, 1665–1677.

Panthou, G., Vischel, T. and Lebel, T. (2014) Recent trends in the regime of extreme rainfall in the Central Sahel. *International Journal of Climatology*, 34, 3998–4006.

Parker, D.J., Burton, R., Diongue-Niang, A., Ellis, R., Felton, M., Taylor, C., Thorncroft, C., Bessemoulin, P. and Tompkins, A. (2005a) The diurnal cycle of the West African monsoon circulation. *Quarterly Journal of the Royal Meteorological Society*, 131, 2839–2860.

Parker, D.J., Fink, A., Janicot, S., Ngamini, J.-B., Douglas, M., Afiesimama, E., Agusti-Panareda, A., Beljaars, A., Dide, F., Diedhiou, A., Lebel, T., Polcher, J., Redelsperger, J.-L., Thorncroft, C. and Wilson, G.A. (2008) The Amma Radiosonde Program and its Implications for the Future of Atmospheric Monitoring Over Africa. *Bulletin of the American Meteorological Society*, 89(7), 1015–1028. http://dx.doi.org/10.1175/2008bams2436.1.

Parker, D.J., Thorncroft, C.D., Burton, R.R. and Diongue-Niang, A. (2005b) Analysis of the African easterly jet, using aircraft observations from the JET2000 experiment. *Quarterly Journal of the Royal Meteorological Society*, 131, 1461–1482.

Parker, M.D. and Johnson, R.H. (2004) Structures and dynamics of quasi-2d mesoscale convective systems. *Journal of the Atmospheric Sciences*, 61, 545–567.

Petch, J., Brown, A. and Gray, M. (2002) The impact of horizontal resolution on the simulations of convective development over land. *Quarterly Journal of the Royal Meteorological Society*, 128, 2031–2044.

Peters, K., Hohenegger, C. and Klocke, D. (2019) Different representation of mesoscale convective systems in convection-permitting and convection-parameterizing NWP models and its implications for large-scale forecast evolution. *Atmosphere*, 10, 503.

Provod, M., Marsham, J.H., Parker, D.J. and Birch, C.E. (2016) A characterization of cold pools in the West African Sahel. *Monthly Weather Review*, 144, 1923–1934.

Rienecker, M.M., Suarez, M.J., Gelaro, R., Todling, R., Bacmeister, J., Liu, E., Bosilovich, M.G., Schubert, S.D., Takacs, L., Kim, G.-K., Bloom, S., Chen, J., Collins, D., Conaty, A., da Silva, A., Gu, W., Joiner, J., Koster, R.D., Lucchesi, R., Molod, A., Owens, T., Pawson, S., Pegion, P., Redder, C.R., Reichle, R., Robertson, F.R., Ruddick, A.G., Sienkiewicz, M. and Woollen, J. (2011) MERRA: NASA's Modern-Era Retrospective Analysis for Research and Applications. *Journal of Climate*, 24(14), 3624–3648. http://dx.doi.org/10.1175/jcli-d-11-00015.1.

Roberts, A.J., Marsham, J.H. and Knippertz, P. (2015) Disagreements in low-level moisture between reanalyses over summertime West Africa. *Monthly Weather Review*, 143, 1193–1211.

Roca, R., Lafore, J.-P., Piriou, C. and Redelsperger, J.-L. (2005) Extratropical dry-air intrusions into the West African monsoon midtroposphere: an important factor for the convective activity over the Sahel. *Journal of the Atmospheric Sciences*, 62, 390–407.

Rotunno, R., Klemp, J.B. and Weisman, M.L. (1988) A theory for strong, long-lived squall lines. *Journal of the Atmospheric Sciences*, 45, 463–485.

Stein, T.H., Parker, D.J., Delanoë, J., Dixon, N., Hogan, R.J., Knippertz, P., Maidment, R.I. and Marsham, J.H. (2011) The vertical cloud structure of the West African monsoon: a 4 year climatology using CloudSat and CALIPSO. *Journal of Geophysical Research: Atmospheres*, 116.

Stephens, G.L., L'Ecuyer, T., Forbes, R., Gettelmen, A., Golaz, J.-C., Bodas-Salcedo, A., Suzuki, K., Gabriel, P. and Haynes, J. (2010) Dreary state of precipitation in global models. *Journal of Geophysical Research: Atmospheres*, 115.

Takemi, T. (2006) Impacts of moisture profile on the evolution and organization of midlatitude squall lines under various shear conditions. *Atmospheric research*, 82, 37–54.

Taylor, C.M., Belušić, D., Guichard, F., Parker, D.J., Vischel, T., Bock, O., Harris, P.P., Janicot, S., Klein, C. and Panthou, G. (2017) Frequency of extreme Sahelian storms tripled since 1982 in satellite observations. *Nature*, 544, 475–478.

Taylor, C.M., Birch, C.E., Parker, D.J., Dixon, N., Guichard, F., Nikulin, G. and Lister, G.M. (2013) Modeling soil moisture-precipitation feedback in the Sahel: importance of spatial scale versus convective parameterization. *Geophysical Research Letters*, 40, 6213–6218.

Taylor, K.E., Stouffer, R.J. and Meehl, G.A. (2012) An overview of CMIP5 and the experiment design. *Bulletin of the American Meteorological Society*, 93, 485–498.

Trenberth, K.E., Stepaniak, D.P., Hurrell, J.W. and Fiorino, M. (2001) Quality of reanalyses in the tropics. *Journal of Climate*, 14, 1499–1510.

Trzeciak, T.M., Garcia-Carreras, L. and Marsham, J.H. (2017) Cross-Saharan transport of water vapor via recycled cold pool outflows from moist convection. *Geophysical Research Letters*, 44, 1554–1563.

Weisman, M.L. (1992) The role of convectively generated rear-inflow jets in the evolution of long-lived mesoconvective systems. *Journal of the Atmospheric Sciences*, 49, 1826–1847.

Weisman, M.L. and Rotunno, R. (2004) "A theory for strong long-lived squall lines" revisited. *Journal of the Atmospheric Sciences*, 61, 361–382.

Weisman, M.L., Skamarock, W.C. and Klemp, J.B. (1997) The resolution dependence of explicitly modeled convective systems. *Monthly Weather Review*, 125, 527–548.

How to cite this article: Bickle ME, Marsham JH, Ross AN, Rowell DP, Parker DJ, Taylor CM. Understanding mechanisms for trends in Sahelian squall lines: Roles of thermodynamics and shear. *Q J R Meteorol Soc*. 2021;147:983–1006. https://doi.org/10.1002/qj.3955